nature immunology

ARTICLES
https://doi.org/10.1038/s41590-021-00921-5

Check for updates

Heme catabolism by tumor-associated macrophages controls metastasis formation

Francesca Maria Consonni[1,2], Augusto Bleve[2], Maria Grazia Totaro[1], Mariangela Storto[1], Paolo Kunderfranco[1], Alberto Termanini[1], Fabio Pasqualini[1], Chiara Alì[2], Chiara Pandolfo[2], Francesco Sgambelluri[3], Giulia Grazia[3], Mario Santinami[4], Andrea Maurichi[4], Massimo Milione[5], Marco Erreni[1], Andrea Doni[1], Marco Fabbri[6], Laura Gribaldo[6], Eliana Rulli[7], Miguel Parreira Soares[8], Valter Torri[7], Roberta Mortarini[3], Andrea Anichini[3] and Antonio Sica[1,2] ✉

Although the pathological significance of tumor-associated macrophage (TAM) heterogeneity is still poorly understood, TAM reprogramming is viewed as a promising anticancer therapy. Here we show that a distinct subset of TAMs (F4/80^{hi}CD115^{hi}C3aR^{hi}CD88^{hi}), endowed with high rates of heme catabolism by the stress-responsive enzyme heme oxygenase-1 (HO-1), plays a critical role in shaping a prometastatic tumor microenvironment favoring immunosuppression, angiogenesis and epithelial-to-mesenchymal transition. This population originates from F4/80$^+$HO-1$^+$ bone marrow (BM) precursors, accumulates in the blood of tumor bearers and preferentially localizes at the invasive margin through a mechanism dependent on the activation of Nrf2 and coordinated by the NF-κB1–CSF1R–C3aR axis. Inhibition of F4/80$^+$HO-1$^+$ TAM recruitment or myeloid-specific deletion of HO-1 blocks metastasis formation and improves anticancer immunotherapy. Relative expression of HO-1 in peripheral monocyte subsets, as well as in tumor lesions, discriminates survival among metastatic melanoma patients. Overall, these results identify a distinct cancer-induced HO-1$^+$ myeloid subgroup as a new antimetastatic target and prognostic blood marker.

Cancers promote immunological stresses that induce alterations of the myelopoietic output, defined as emergency myelopoiesis[1–3], which lead to the generation of different myeloid populations endowed with tumor-promoting activities[4]. Among these, TAMs represent the final commitment of protumoral reprogramming of the myeloid lineage. TAMs promote tumor development by favoring angiogenesis, immunosuppression, tissue remodeling and metastasis formation[5,6]. These functions are cooperatively fulfilled by heterogeneous macrophage subsets stemming from a multistep process encompassing altered myelopoiesis, intratumoral recruitment of TAM progenitors and their functional diversion in response to microenvironmental signals[7]. Emerging evidence indicates that tumor-derived signals can actively reprogram macrophage metabolism[8] and that distinct metabolic traits discriminate different macrophage differentiation and activation programs[9]. In this setting, while selected transcription factors such as cEBPβ and RORγ (*Rorc*) regulate emergency myelopoiesis and contribute to the heterogeneous expansion of suppressive myeloid populations[4], nuclear factor-κB1 (NF-κB1, also known as *p50*) stimulates neutrophil production by induction of c/EBPα[10] and promotes resolution of inflammation by diversion of monocytes/macrophages toward a resolving anti-inflammatory M2-like phenotype[11–13]. However, even though the resolution phase of acute inflammatory response is crucial for tissue homeostasis and is supported by an adaptation of hematopoietic output to inflammatory insults, no information is yet available on the mechanisms linking altered myelopoiesis to macrophage shift toward an alternative M2-polarized state, as observed in persistent infections and cancer[11–13].

Based on this premise, we investigated the heterogeneity of emerging myeloid populations in response to cancer-related inflammation and observed that cancer growth promotes systemic expansion of a myeloid subset endowed with high heme metabolism[14]. The expansion of both circulating HO-1$^+$ monocytes and HO-1^{hi} TAMs is associated with poor prognosis in both preclinical tumor models and patients with melanoma, and is dependent on the targetable molecular axis p50 NF-κB–CSF-R1–C3aR–Nrf2–HO-1 that controls their differentiation, expansion and recruitment at the tumor site.

Results

p50 NF-κB controls the prometastatic activity of a distinct TAM subset. Given the overlapping traits between lipopolysaccharide (LPS)-tolerant macrophages and TAMs, which include nuclear accumulation of p50 NF-κB and M2-related features[11–13], and based on the observation that acute stimulation of monocytes/macrophages with classic M1 polarization signals (for example, LPS) reduces their chemotactic reactivity to CC chemokines[15], we first compared the chemotactic responsiveness of wild-type (WT) and

---

[1]Humanitas Clinical and Research Center, IRCCS, Rozzano, Milan, Italy. [2]Department of Pharmaceutical Sciences, University of Piemonte Orientale 'A. Avogadro', Novara, Italy. [3]Department of Research, Human Tumors Immunobiology Unit, Fondazione IRCCS Istituto Nazionale Dei Tumori, Milan, Italy. [4]Department of Surgery, Melanoma and Sarcoma Unit, Fondazione IRCCS Istituto Nazionale Dei Tumori, Milan, Italy. [5]First Division of Pathology, Department of Pathology and Laboratory Medicine, Fondazione IRCCS Istituto Nazionale dei Tumori, Milan, Italy. [6]European Commission, Joint Research Centre (JRC), Ispra, Italy. [7]Istituto di Ricerche Farmacologiche Mario Negri IRCCS, Milan, Italy. [8]Instituto Gulbenkian de Ciência, Oeiras, Portugal. ✉e-mail: antonio.sica@uniupo.it

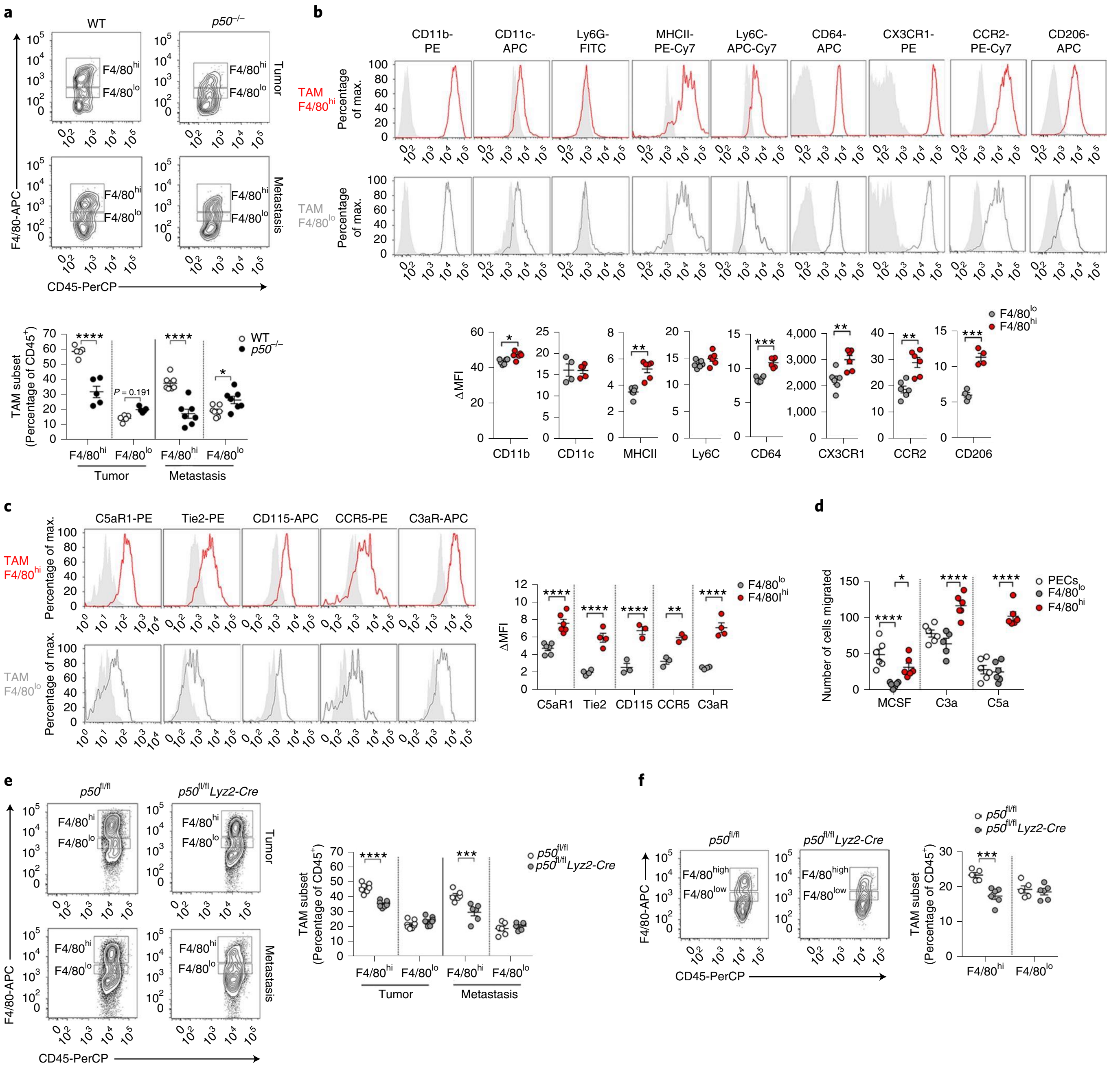

Fig. 1 | Identification of two distinct F4/80^{hi} and F4/80^{lo} TAM subsets in primary and metastatic tumor lesions. **a**, Representative fluorescent activated cell sorter (FACS) plot of F4/80^{hi} and F4/80^{lo} TAMs in primary and metastatic MN/MCA1 tumors, in WT and *p50*$^{-/-}$ mice. $n = 5$ (tumor) and $n = 7$ (metastasis) animals per genotype. **b**,**c**, Expression levels of myeloid markers and chemotactic receptors in F4/80^{hi} (top) and F4/80^{lo} (bottom) TAMs. **b**, $n = 6$ (CD11b, MHCII, Ly6C, CD64, CX3CR1, CCR2), $n = 5$ (CD11c F4/80^{hi}) and $n = 4$ (CD11c F4/80^{lo}, CD206) mice. **c**, $n = 6$ (C5aR1), $n = 4$ (Tie2, C3aR) and $n = 3$ (CCR5, CD115) mice. **d**, Boyden chamber migration assay of F4/80^{hi} and F4/80^{lo} TAMs, FACS sorted from WT sarcoma in comparison with PECs. $n = 6$ animals per group. **e**, Representative FACS plot and frequency of F4/80^{hi} and F4/80^{lo} TAMs in primary lung tumors and metastases of *p50*$^{fl/fl}$ and *p50*$^{fl/fl}$*Lyz2-Cre* MN/MCA1-bearing mice. $n = 7$ (tumor) and $n = 5$ (metastasis) mice per genotype. **f**, Representative FACS plot and frequency of F4/80^{hi} and F4/80^{lo} TAMs in primary tumors of *p50*$^{fl/fl}$ and *p50*$^{fl/fl}$*Lyz2-Cre* B16-bearing mice. $n = 6$ mice per genotype. **a**,**e**, Data are representative of five independent experiments. **f**, Representative experiment from $n = 2$ performed. **b**–**d**, Data shown are pooled from $n = 2$ independent experiments. **a**–**f**, Data are expressed as mean ± s.e.m. $^{*}P < 0.05$, $^{**}P < 0.01$, $^{***}P < 0.001$, $^{****}P < 0.0001$ between selected relevant comparisons. Two-way analysis of variance (ANOVA) with Šidák's multiple comparisons test.

p50$^{-/-}$ peritoneal-elicited macrophages (PECs) in response to the anaphylatoxins C3a and C5a[16]. While both genetic backgrounds of macrophages expressed the chemotactic complement receptors C3aR and C5aR1 (also known as CD88) to a similar extent (Extended Data Fig. 1a), *p50*$^{-/-}$ PECs poorly migrated in response to C5a and C3a in vitro and showed impaired extracellular signal-regulated kinase (ERK)1/2 phosphorylation[17] (Extended Data Fig. 1b–d). Moreover, unlike LPS-activated PECs (M/L), LPS-tolerant PECs (L/L) recovered their chemotactic responsiveness and ERK1/2 phosphorylation (Extended Data Fig. 1e,f) in a p50-dependent

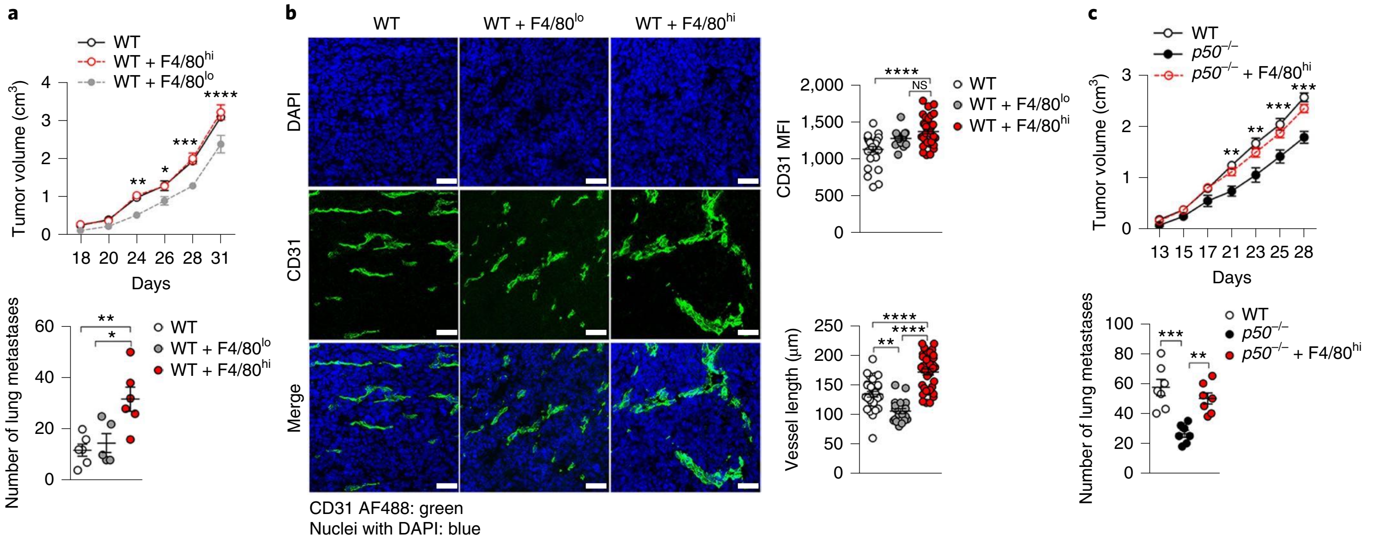

Fig. 2 | Distinct effects of F4/80$^{\text{hi}}$ and F4/80$^{\text{lo}}$ TAMs on metastasis formation and tumor angiogenesis. a, Tumor growth (top) and lung metastasis (bottom) in WT MN/MCA1 tumor-bearing mice adoptively transferred with F4/80$^{\text{hi}}$ or F4/80$^{\text{lo}}$ TAMs. $n=6$ (WT, WT + F4/80$^{\text{hi}}$) and $n=5$ (WT + F4/80$^{\text{lo}}$) mice. **b**, Immunofluorescence analysis, vessel length and relative quantification of CD31^{+} cells in MN/MCA1 tumors. $n=6$ (WT, WT + F4/80$^{\text{hi}}$) and $n=4$ (WT + F4/80$^{\text{lo}}$) mice. Five random fields per sample were counted. **c**, Tumor growth (top) and number of lung metastases (bottom) in *p50*$^{-/-}$ MN/MCA1 tumor-bearing mice adoptively transferred with WT F4/80$^{\text{hi}}$ TAMs. $n=7$ mice per group. Representative images are shown. Scale bars, 10 µm. **a**–**c**, Data are representative of two independent experiments and are expressed as mean ± s.e.m. $^{*}P<0.05$, $^{**}P<0.01$, $^{***}P<0.001$, $^{****}P<0.0001$ between selected relevant comparisons. **a**,**c**, Two-way ANOVA with Šidák's multiple comparisons test and one-way ANOVA. **b**, One-way ANOVA and Kruskal–Wallis test with Dunn's multiple comparisons test. NS, not significant.

manner (Extended Data Fig. 1g), indicating that p50 accumulation in tolerant macrophages restores ERK1/2 signaling.

Next, we sought to determine the role of p50 in TAM recruitment in vivo. While implantation of the fibrosarcoma MN/MCA1 in WT mice gave rise to readily identifiable F4/80$^{\text{lo}}$ and F4/80$^{\text{hi}}$ TAMs, we observed a selective reduction of the F4/80$^{\text{hi}}$ subset in *p50*$^{-/-}$ mice (Fig. 1a). Both subsets expressed the myeloid markers Ly6C, CD11c and CD11b and the chemokine receptors CX3CR1 and CCR2, but they were negative for the granulocytic marker Ly6G (Fig. 1b). Importantly, in comparison with F4/80$^{\text{lo}}$ TAMs, F4/80$^{\text{hi}}$ TAMs expressed higher levels of MHCII, CD64, CD206 (Fig. 1b), CCR5, the angiopoietin receptor Tie2 (Fig. 1c)—typically expressed by a proangiogenic monomacrophage subset[18], the complement receptors C3aR and C5aR1 (CD88) and the macrophage colony-stimulating factor (M-CSF) receptor (also known as CSF1R, CD115), these last governing, respectively, recruitment and activation pathways (C3a and C5a)[16] and differentiation and chemoattraction (M-CSF)[19] of myelomonocytic cells. The increased migration of F4/80$^{\text{hi}}$ TAMs to C5a, C3a and M-CSF (Fig. 1d) was confirmed in vivo by their higher intratumoral accumulation in both MN/MCA1 fibrosarcoma (primary and lung metastasis) (Fig. 1e) and melanoma (B16F10) (Fig. 1f), which reduced following myeloid-specific ablation of p50 NF-κB (*p50*$^{\text{fl/fl}}$*Lyz2-cre* mice).

Coinjection of F4/80$^{\text{hi}}$-sorted TAMs and MN/MCA1 cells increased metastasis formation (Fig. 2a, bottom), expression of the endothelial marker CD31^{+} and tumor vessel length (Fig. 2b) without affecting primary tumor growth (Fig. 2a, top). In contrast, coinjection of F4/80$^{\text{lo}}$ TAMs reduced primary tumor growth (Fig. 2a, top) and vessel length (Fig. 2b) without affecting metastasis formation (Fig. 2a, bottom). Lastly, adoptive transfer of F4/80$^{\text{hi}}$ TAMs in *p50*$^{-/-}$ mice[20] restored tumor growth and lung dissemination (Fig. 2c), indicating that F4/80$^{\text{hi}}$ TAMs are both proangiogenic and prometastatic. These results demonstrate that p50 NF-κB finely modulates the chemotactic responses of macrophages, favoring the accumulation of a F4/80$^{\text{hi}}$ TAM population in the tumor lesion.

M-CSF and C3 promote accumulation of protumoral F4/80$^{\text{hi}}$ TAMs. We next investigated the accumulation pathways of TAMs in vivo by interference with M-CSF receptor (CSF1R) signaling[19]. Anti-CSF1R treatment of MN/MCA1-bearing mice markedly reduced F4/80$^{\text{hi}}$CD115$^{\text{hi}}$ TAMs in primary and metastatic lesions (Fig. 3a), tumor growth (Fig. 3b) and metastasis formation (Extended Data Fig. 2a), number of intratumoral CD31^{+} endothelial cells and microvasculature density (Fig. 3c), number of intrametastatic CD31^{+} endothelial cells (Extended Data Fig. 2b) and F4/80$^{\text{hi}}$ TAM proliferation (Fig. 3d). The effects of anti-CSF1R treatment were further validated in the B16 melanoma model (Fig. 3e,f). Similarly, F4/80$^{\text{hi}}$ TAMs were reduced in both primary and metastatic lesions of *C3*$^{-/-}$ MN/MCA1-bearing mice, a phenomenon accompanied by decreased tumor growth, metastasis formation, number of CD31^{+} endothelial cells and vessel length (Fig. 3g–i and Extended Data Fig. 2c,d. These results were reproduced in B16-bearing mice (Fig. 3j,k), supporting the tumor-promoting role of complement factors[21,22].

In an effort to correlate the phenotypes of metastasis formation with abnormalities of tumor vasculature, vessel leakage, pericyte coverage and collagen IV (COL IV), a major constituent of the vascular basement membrane, were evaluated in different genotypes. As ascertained by colocalization of intravenously injected 40-*kDa* dextran-fluorescein isothiocyanate (FITC) and CD31^{+} vessels, or CD31^{+} with either COL IV or α-SMA, tumors of *C3*$^{-/-}$ mice showed augmented vessel leakiness and diminished vessel coverage compared to WT (Extended Data Fig. 2e). In contrast, anti-CSF1R treatment did not affect vessel leakage while decreasing vessel coverage (Extended Data Fig. 2e). Thus, M-CSF and C3 combine to drive the accumulation of CD115$^{\text{hi}}$C3aR$^{\text{hi}}$F4/80$^{\text{hi}}$ TAMs, increasing tumor growth, angiogenesis and metastasis formation.

F4/80$^{\text{hi}}$ TAMs express high levels of HO-1 at the invasive tumor margin. To obtain deeper insights into the biology of TAMs, we next performed genome-wide analysis of TAM subsets. Principal component analysis (PCA) revealed profound differences between the

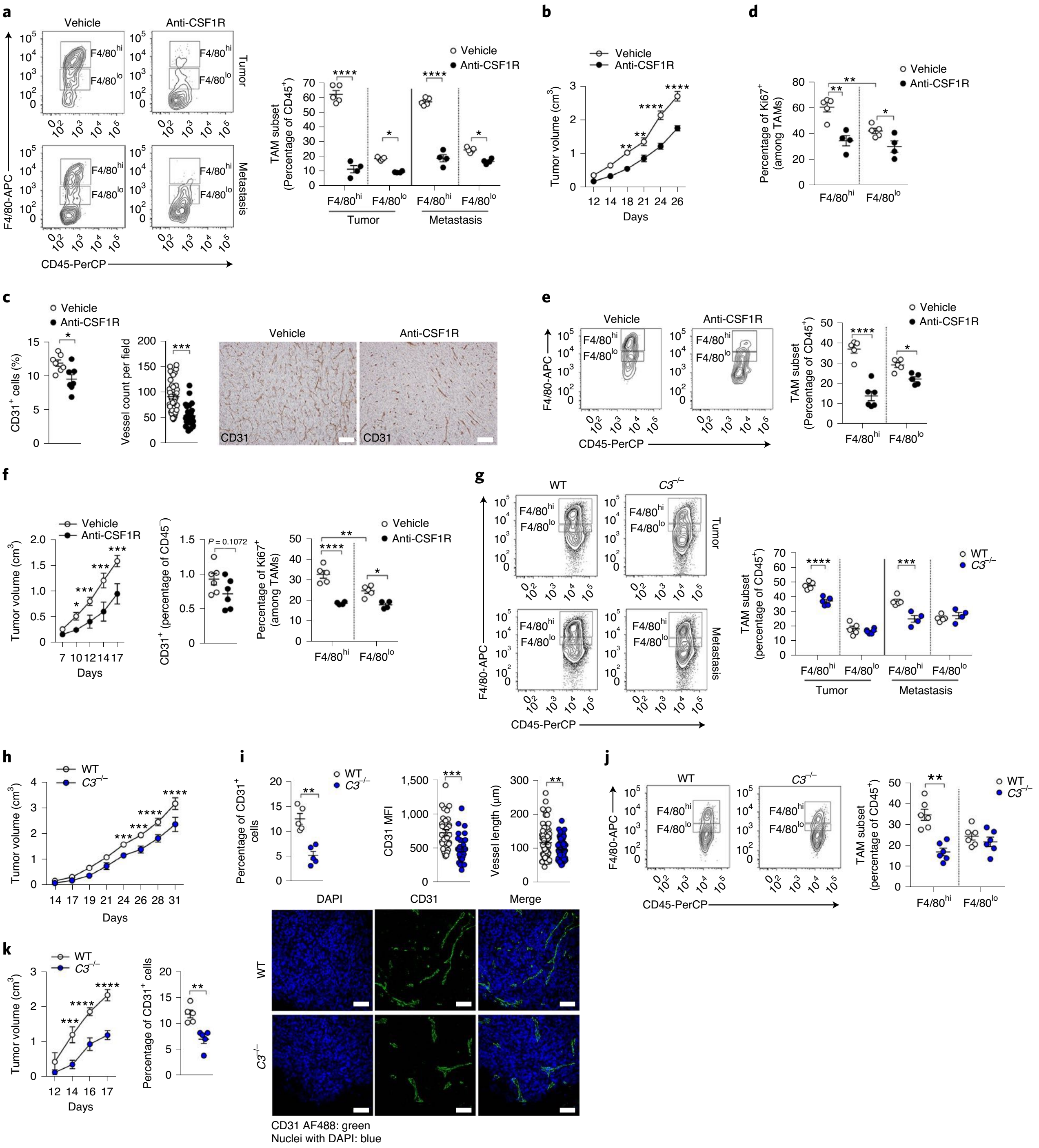

Fig. 3 | Pathways of F4/80hi TAM accumulation and contribution to tumor development. **a**, Frequency of F4/80hi and F4/80lo TAMs in vehicle- or anti-CSF1R-treated tumor-bearing mice. $n=5$ (vehicle) and $n=4$ (anti-CSF1R) mice. **b**, Tumor growth in WT MN/MCA1-bearing mice treated with vehicle or anti-CSF1R. **c**, FACS quantification (left), vessel length (center) and immunohistochemical analysis of CD31+ cells (right). Representative images are shown; 30 random fields per sample were counted. Scale bars, 10 μm. $n=7$ (vehicle) and $n=5$ (anti-CSF1R) mice. **d**, TAM proliferation in primary tumors from anti-CSF1R-treated mice. $n=5$ (vehicle) and $n=4$ (anti-CSF1R) mice. **e**, FACS plot and frequency of TAM subsets in vehicle- or anti-CSF1R-treated B16-bearing mice. $n=5$ mice per group. **f**, B16 tumor growth, percentage of CD31+ endothelial cells and proliferation rates of TAM subsets in WT mice treated with vehicle or anti-CSF1R. Left and center, $n=6$ mice per group; right, $n=5$ (vehicle) and $n=4$ (anti-CSF1R) mice. **g**, Representative dot plot and frequency of F4/80hi and F4/80lo TAM subsets in WT or *C3*−/− MN/MCA1-bearing mice. Tumor, $n=5$; metastasis, $n=5$ (WT) and $n=4$ (*C3*−/−) mice. **h**, Tumor growth in WT or *C3*−/− MN/MCA1-bearing mice. $n=7$ mice per genotype. **i**, FACS quantification (top) and immunofluorescence analysis of CD31+ cells and vessel length (bottom). Representative images are shown; 30 random fields per sample were counted. Scale bars, 10 μm. $n=5$ mice per genotype. **j**, Representative dot plot and frequency of F4/80hi and F4/80lo TAM subsets in WT and *C3*−/− B16-bearing mice. $n=6$ mice per genotype. **k**, Tumor growth of B16 melanoma in WT and *C3*−/− mice (left); FACS quantification of CD31+ cells (right). $n=5$ mice per genotype. **a**,**b**, Data are representative of three independent experiments. **c** (left),**d**,**g**,**h**, Data are representative of two independent experiments. **c** (right),**e**,**f**,**i**–**k**, One experiment was performed. Data are mean ± s.e.m. $^{*}P<0.05$, $^{**}P<0.01$, $^{***}P<0.001$, $^{****}P<0.0001$ between selected relevant comparisons. **a**,**b**,**d**,**e**–**h**, Two-way ANOVA with Šidák's multiple comparisons test. **c**,**f**,**j**,**k**, Two-tailed unpaired Student's *t*-test or Mann–Whitney *U*-test.

transcriptional landscape of F4/80^{hi} and F4/80^{lo} TAMs (Fig. 4a,b). Pairwise differential analysis between F4/80^{hi} and F4/80^{lo} TAMs and PECs identified a set of 5,587 differentially modulated genes (Fig. 4b and Supplementary Table 1), including the markers of poor prognosis in breast cancer *SIGLEC1* and *CCL8* (ref. [23]). Specifically, gene ontology (GO) enrichment analysis showed remarkable differences in iron metabolism as demonstrated by differential expression of iron-regulated genes (Fig. 4c,d). Since the vast majority of iron is contained within the protoporphyrin ring of heme[24] and, given that HO-1-driven heme catabolism exerts potent antioxidant, cytoprotective and immunoregulatory activities[14,25] in various tumors[26], we measured gene expression levels of the alternative activation marker HO-1 (*Hmox1*)[27]. F4/80^{hi} TAMs expressed higher levels of *Hmox1* messenger RNA and protein (Fig. 4e, left).

Based on this evidence, TAMs were analyzed for mRNA levels of genes involved in both heme biosynthesis (*Alas1*, *Alad*, *Urod*, *Cpox*, *Fech*, *Ppox*, *Hmbs*)[28] and endocytic supply (CD163, a regulated hemoglobin scavenger receptor with a role in the anti-inflammatory response). Although the two populations of TAMs did not show significant differences in expression levels of heme biosynthetic genes (*Alas1*, *Alad*, *Urod*, *Cpox*, *Fech*, *Ppox*, *Hmbs*) (not shown), F4/80^{hi}HO-1^{hi} TAMs displayed increased CD163 expression (Fig. 4e, right), indicating CD163-mediated haptoglobin-hemoglobin endocytosis as their primary route of heme feeding.

We next determined the topographical localization of HO-1$^+$ TAMs as a potential indicator of prognosis[2]. Confocal microscopy and immunohistochemical analysis of MN/MCA1 tumors showed HO-1$^-$ TAMs to be preferentially localized in inner tumor areas whereas HO-1$^+$ TAMs accumulated at their invasive margin (Extended Data Fig. 3a), consistent with neoangiogenesis and cancer cell spread[29]. This observation was confirmed in human metastatic melanoma lesions where CD68$^+$ TAMs, coexpressing the alternative M2 activation markers HO-1 and CD163 (ref. [3]), accumulated preferentially at the invasive tumor edge (Extended Data Fig. 3b). Therefore, the invasive margin of primary and metastatic tumors is the preferred site of accumulation of a distinct population of macrophages endowed with high heme metabolism.

Myeloid-specific heme catabolism orchestrates metastasis formation. To determine whether HO-1 expression by F4/80^{hi} TAMs contributes to tumor development, we used *Hmox1*$^{fl/fl}$*Lyz2-Cre* mice in which *Hmox1* is specifically deleted in the myeloid compartment. While ablation of HO-1 did not affect primary MN/MCA1 tumor growth (Fig. 5a, left), it reduced lung metastasis formation (Fig. 5a, right and Extended Data Fig. 3c), frequency of F4/80^{hi} TAMs (Fig. 5b, left) and CD31$^+$ endothelial cell numbers in both primary and metastatic lung tumors (Fig. 5c and Extended Data Fig. 3d). Of note, the reduced number of F4/80^{hi} TAMs observed under HO-1-deficient conditions was paralleled by the reduced surface expression of both M-CSF receptor (CD115) and cell proliferation (Fig. 5b, right).

Similarly with *C3*$^{-/-}$ mice, as compared to *Hmox1*$^{fl/fl}$ mice, an augmented vascular leakage was observed in *Hmox1*$^{fl/fl}$*Lyz2-Cre* mice (Extended Data Fig. 3e top) that was accompanied by decreased colocalization of CD31$^+$ and COL IV (Extended Data Fig. 3e, bottom left). However, no differences were observed in colocalization between CD31$^+$ and α-SMA (Extended Data Fig. 3e, bottom right), indicating higher vessel density as the prominent prometastatic determinant. In agreement, evaluation of expression levels of angiogenic molecules in CD31$^+$ cells and TAMs (Extended Data Fig. 3f) showed higher levels of hypoxia-inducible factor 1α (HIF1α), vascular endothelial growth factor (VEGF) and VEGF receptor (VEGFR) in both primary tumor (top) and lung metastasis (bottom) of *Hmox1*$^{fl/fl}$ tumor bearing mice, as compared to *Hmox1*$^{fl/fl}$*Lyz2-Cre* mice. Furthermore, HO-1 deletion promoted an M2 (TNF^{lo}CD206^{hi}p-STAT1^{lo}p-STAT3^{hi}p-STAT6^{hi}) to M1 (TNFα^{hi}CD206^{lo}p-STAT1^{hi}p-STAT3^{lo}p-STAT6^{lo}) phenotypic switch of F4/80^{hi} TAMs[3,13] (Fig. 5d) and reactivated the specific immune response, as shown by increased IFNγ and GrzB expression in CD8$^+$ T cells, a higher frequency of effector memory CD8$^+$CD44$^+$CD62L$^-$ cells and an augmented CD8$^+$/CD4$^+$FoxP3$^+$ (regulatory T cell (T$_{reg}$)) ratio (Fig. 5e).

To further investigate the role of HO-1 in metastasis, we first evaluated the number of circulating tumor cells in myeloid-specific proficient and deficient conditions since their presence correlates with poor clinical outcome in several cancers. In agreement with Extended Data Fig. 3c, quantification of circulating MN/MCA1 mCherry$^+$ tumor cells, either by cytofluorimetry or PCR with reverse transcription (RT–PCR) for mCherry gene expression (Fig. 5f), confirmed their reduced levels under HO-1-deficient conditions. In agreement, *Hmox1*/HO-1 deletion correlated with inhibition of tumor cell epithelial-to-mesenchymal transition (EMT), as shown by decreased expression of mesenchymal markers *Cdh2* (encoding N-cadherin), *Twist* (encoding the Twist-related protein 1), *Vim* (encoding vimentin) and *Snai1* (encoding Snail) and enhanced expression of *E-cadherin* and *Epcam* (respectively encoding the epithelial marker E-cadherin and the epithelial cellular adhesion molecule also known as CD36) (Extended Data Fig. 4a). Inhibition of primary and metastatic tumors following myeloid-specific *Hmox1* deletion was confirmed in the B16 melanoma model (Extended Data Fig. 4b) and was paralleled by an M2 (TNF^{lo}, CD206^{hi}) to M1 (TNF^{hi}, CD206^{lo}) phenotypic switch of TAMs and lower frequency of CD31$^+$ cells (Extended Data Fig. 4c), increased number of tumor-infiltrating IFN-γ$^+$CD8$^+$ T cells, enhanced CD8$^+$/T$_{reg}$ cell ratio (Extended Data Fig. 4d) and reduced EMT (Extended Data Fig. 4e).

Since the cytoprotective effect of HO-1 is exerted essentially via the catabolism of cytotoxic labile heme[30] and the generation of carbon monoxide (CO)[14], which acts in a noncell-autonomous manner, we asked whether HO-1$^+$ TAM-mediated production of CO would favor tumor growth. To determine how heme catabolism by HO-1 modulates macrophage activation, we treated M/L or L/L PECs with the HO-1 enzymatic inhibitor zinc protoporphyrin IX (ZnPPIX)[31]. Inhibition of HO-1 enzymatic activity restored expression of the prototypical M1 genes TNF and CXCL10 by L/L, while it downregulated gene expression of M2, IL-10 and CCL22 (ref. [13]) (Extended Data Fig. 4f). Consistent with the observation that deletion of NF-κB1 leads to both aberrant expression of the proinflammatory cytokines TNF and CXCL10 and reduced expression of the anti-inflammatory M2 mediators IL-10 and CCL22 (ref. [13]), the CO-releasing molecule CORM-2 reversed the effects caused by NF-κB1 deletion or inhibition of HO-1 activity (Extended Data Fig. 4g,h). These data indicate that high HO-1 expression in TAMs supports metastasis formation by promotion of tumor angiogenesis, M2 polarization of macrophages, inhibition of CD8$^+$ T cells and EMT transition.

CSF1R guides the expansion of HO-1-expressing myeloid cells. In agreement with NF-κB1 as a regulator of myeloid-specific HO-1$^+$ myeloid populations under LPS-tolerant conditions (Extended Data Fig. 4i), expansion of Ly6C$^{low/-}$F4/80$^+$SiglecF$^-$C5aR1$^+$C3aR$^+$HO-1$^+$ blood cells in fibrosarcoma-bearing mice (Fig. 6a) was prevented by p50 deletion (*p50*$^{-/-}$ mice) (Fig. 6g).

To better investigate the role of p50 NF-κB, CSF1R and C3aR in the generation of HO-1$^+$ myeloid cells, we evaluated expression of the transcription factor Nrf2, a well-known inducer of HO-1-expressing hemophagocytic macrophages[32]. In line with the higher expression of HO-1, TAM F4/80^{hi} expressed higher levels of Nrf2 (Extended Data Fig. 5a, left), which was reduced by both anti-CSF1R treatment and C3 depletion (*C3*$^{-/-}$ mice) (Extended Data Fig. 5a, middle). Further, estimation of HO-1 mean fluorescence intensity (MFI) showed reduced Nrf2 levels following either

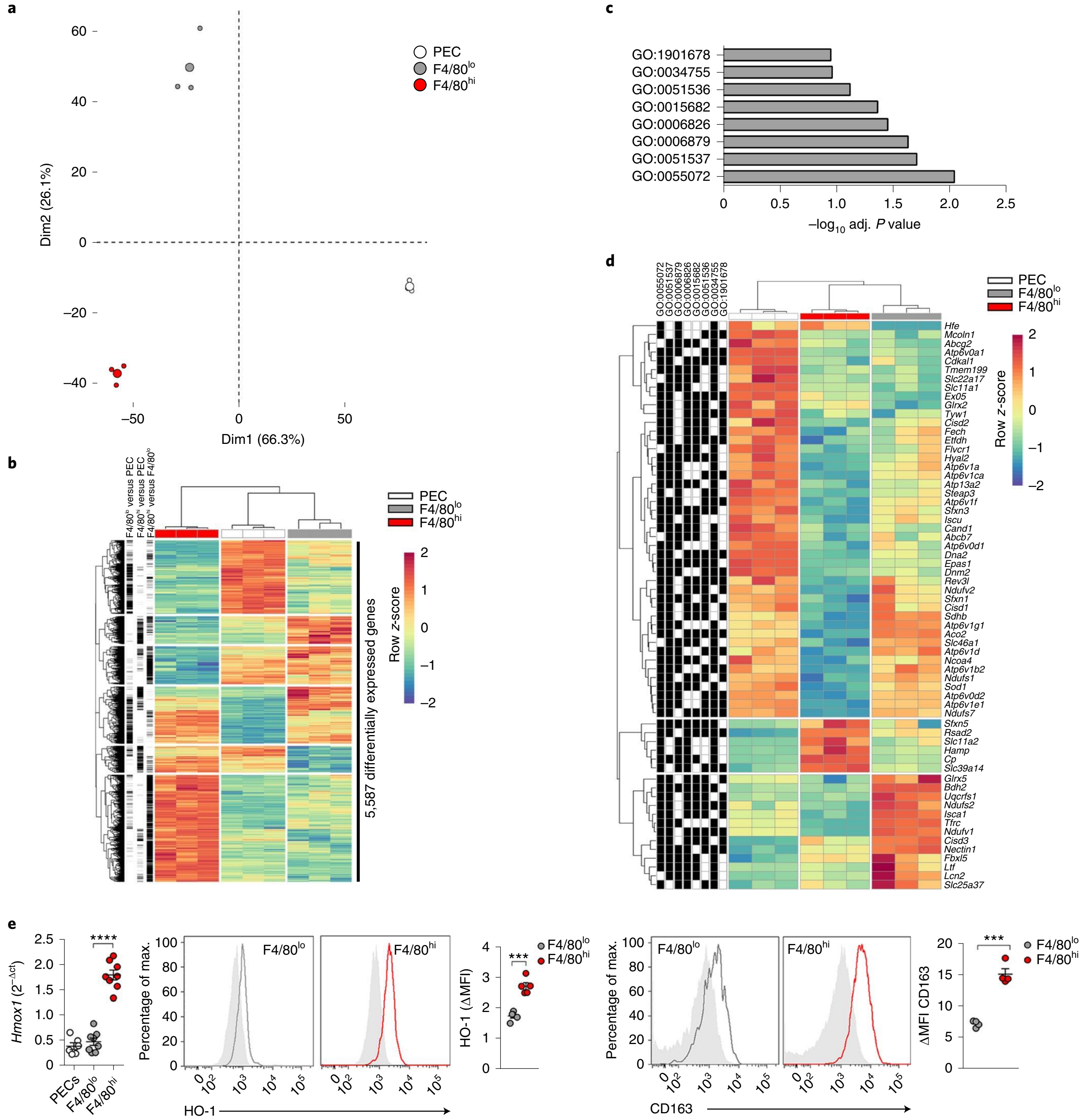

Fig. 4 | Genomic analysis of HO-1⁺ TAMs. a, PCA of genes in PECs and F4/80^{lo} and F4/80^{hi} TAMs. Colors indicate group identity: white, PECs; gray, F4/80^{lo} TAMs; red, F4/80^{hi} TAMs ($n = 9$). Averaged sample variance for each group is represented by large circles. Percentage of variance for each principal component (Dim1, Dim2) is indicated on the axes. **b**, Heatmap showing hierarchical clustering of 5,587 significantly differentially expressed genes among PECs and F4/80^{lo} and F4/80^{hi} samples. Adjusted $P \leq 0.05$; false discovery rate correction for multiple testing. Scale bar representing expression *z*-score is shown on the right. Black dots on the left indicate whether a gene was found significantly differentially expressed in the pairwise comparison shown above. **c**, Bar plot showing representative GO gene set found significantly enriched (adjusted (adj.) $P \leq 0.1$) among 5,587 significantly differentially expressed genes. The gene set was retrieved from the Molecular Signatures Database (c5.bp.v6.2). **d**, Heatmap showing hierarchical clustering of 64 significantly differentially expressed genes belonging to the gene set categories shown in **c**. Scale bar representing expression *z*-score is shown on the right. Black dots on the left indicate whether a gene was present in the gene set categories shown above. **e**, mRNA levels of HO-1 in PECs and F4/80^{lo} and F4/80^{hi} TAMs (left); shown are pooled data from $n = 3$ independent experiments with $n = 3$ animals per group; representative FACS plot and quantification of HO-1 expression by F4/80^{hi} and F4/80^{lo} TAMs in MN/MCA1 tumors (middle). $n = 5$ mice; data are representative of three independent experiments; representative FACS plot and quantification of CD163 expression by F4/80^{hi} and F4/80^{lo} TAMs in MN/MCA1 tumors (right). $n = 4$ mice; data are representative of $n = 2$ independent experiments. Data are mean ± s.e.m. $^{***}P < 0.001$, $^{****}P < 0.0001$ between selected relevant comparisons. **e**, One-way ANOVA or two-tailed unpaired Student's *t*-test.

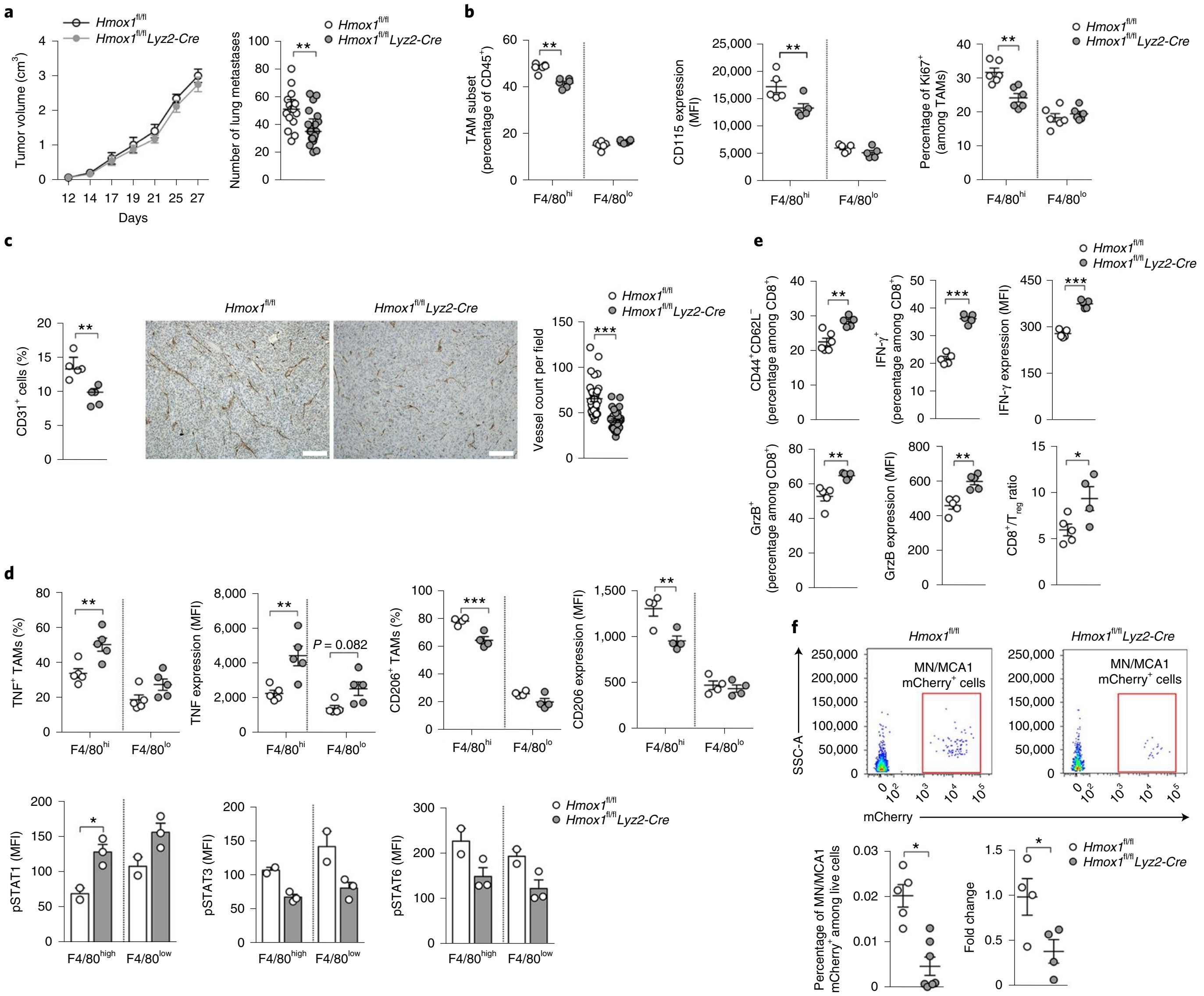

Fig. 5 | Role of myeloid-specific HO-1 in cancer development. **a**, MN/MCA1 growth (left, $n=7$ mice per genotype) and lung metastases (right) in *Hmox1*$^{fl/fl}$ ($n=15$) mice and *Hmox1*$^{fl/fl}$*Lyz2-Cre* ($n=21$) mice. **b**–**e**, Leukocyte infiltration in *Hmox1*$^{fl/fl}$ and *Hmox1*$^{fl/fl}$*Lyz2-Cre* MN/MCA1-bearing mice. **b**, Frequency of TAM subsets, CD115 expression and proliferation rates of TAM subsets in *Hmox1*$^{fl/fl}$ and *Hmox1*$^{fl/fl}$*Lyz2-Cre* MN/MCA1-bearing mice; $n=6$ mice per genotype. **c**, FACS and immunohistochemical analysis of CD31$^+$ cells; $n=5$ mice per genotype. Representative images are shown, with 30 random fields per sample counted. Scale bars, 10 µm. **d**, Expression of TNF$^+$ and CD206$^+$ (top, $n=5$ mice per genotype) and pSTAT1, pSTAT3 and pSTAT6 (bottom, $n=2$ mice (*Hmox1*$^{fl/fl}$) and $n=3$ mice (*Hmox1*$^{fl/fl}$*Lyz2-Cre*)) in TAM subsets. **e**, IFN-γ$^+$ and GrzB$^+$ in CD8$^+$ T cells, effector memory (CD44$^+$CD62L$^-$) CD8$^+$ T cells and CD8$^+$/T$_{reg}$ ratio; $n=5$–6 mice per genotype. **f**, Top and bottom left: representative FACS plot and quantification of circulating MN/MCA1 mCherry$^+$ tumor cells in blood of *Hmox1*$^{fl/fl}$ and *Hmox1*$^{fl/fl}$*Lyz2-Cre* MN/MCA1-bearing mice 20 days after injection of tumor cells; $n=5$ mice (*Hmox1*$^{fl/fl}$) and $n=7$ mice (*Hmox1*$^{fl/fl}$*Lyz2-Cre*). Bottom right: blood was collected from $n=4$ *Hmox1*$^{fl/fl}$ and $n=4$ *Hmox1*$^{fl/fl}$*Lyz2-Cre* MN/MCA1-bearing mice 20 days after injection of tumor cells and analyzed by RT–PCR for mCherry expression. **a** (left),**b**, Data are representative of three independent experiments. **a** (right), Data from pooled ($n=3$) experiments. **c**,**d** (top), Data are representative of two independent experiments. **d** (bottom),**f**, One experiment was performed. Data are mean ± s.e.m. $^*P<0.05$, $^{**}P<0.01$, $^{***}P<0.001$ between selected relevant comparisons. **a**–**d**, Two-way ANOVA with Šidák's multiple comparisons test. **b**,**e**,**f**, Two-tailed unpaired Student's *t*-test or Mann–Whitney *U*-test.

anti-CSF1R treatment, C3 depletion (*C3*$^{-/-}$ mice) or p50 NF-κB depletion (*p50*$^{-/-}$ mice) (Extended Data Fig. 5a, right), indicating their regulation of *Hmox1* transcription.

Further, in accordance with the M-CSF-dependent expansion of F4/80^{hi} TAMs, depletion of either p50 NF-κB or C3 decreased the expression levels of CSF1R (CD115) by these cells (Extended Data Fig. 5b). In agreement, in vitro treatment of PECs with C3 enhanced the expression of both Nrf2 and HO-1 in a p50 NF-κB-dependent manner (Extended Data Fig. 5c), indicating that additional circuits, independent of the C3–p50 axis, can support the levels of Nrf2 in vivo (Extended Data Fig. 5a, center), while M-CSF-induced expression of both Nrf2 and HO-1 was reduced by p50 and C3 ablation (Extended Data Fig. 5d). The induction of C3aR and CD115 by their reciprocal ligands further supported their functional interplay (Extended Data Fig. 5c,d).

Corroborating this finding, in vitro treatment of WT BM-derived macrophages (BM-DMs) with either C3 or M-CSF enhanced the expression of both Nrf2 and HO-1 (Extended Data Fig. 5e). To confirm the role of Nrf2 in HO-1 induction, we next took advantage of Nrf2-deficient (*Nfe2l2*$^{-/-}$) BM-DMs. Consistently, the induced expression of HO-1, by either C3 or M-CSF was reduced following Nrf2 ablation (Extended Data Fig. 5e, right). Accordingly, in vivo treatment of fibrosarcoma-bearing WT mice with brusatol, a specific Nrf2 inhibitor[33], reduced lung metastasis formation in WT mice while this effect was lost in either C3-, p50-, M-CSF- or myeloid-specific HO-1 depletion (Extended Data Fig. 5f). Moreover, while brusatol did not affect the frequency of F4/80$^{\mathrm{hi}}$ TAMs, it reduced their expression of HO-1 only in WT mice (Extended Data Fig. 5g, top). This finding was consistently mirrored by the reduced frequency of HO-1-expressing granulocyte/monocyte progenitors (GMPs) within the lineage-negative and c-Kit-positive hematopoietic cells (Lin$^-$c-Kit$^+$, LK) fraction in response to brusatol treatment (Extended Data Fig. 5g, bottom).

To track the ontogeny of HO-1$^+$ myeloid cells, lethally irradiated CD45.2$^+$ mice were adoptively transferred with BM cells derived from CD45.1$^+$ mice and, 8 weeks later, injected with MN/MCA1 cells. The vast majority (>90%) of immune cells in both primary tumors and blood were BM donor-derived (CD45.1), among which CD45.1$^+$ TAMs displayed higher levels of HO-1 and CCR2 expression (Fig. 6b). We next sought to determine the commitment of Lin$^-$Sca-1$^+$ hematopoietic progenitors into common myeloid progenitors (CMPs), GMPs or megakaryocyte/erythroid progenitors (MEPs). Whereas cancer growth increased the frequency of HO-1$^+$ GMPs (Fig. 6c), anti-CSF1R treatment or NF-κB1 deletion reduced HO-1-expressing GMPs and Gr1$^-$CD11b$^+$F4/80$^+$ BM cells within the LK fraction (Fig. 6d,e).

In contrast, C3 deletion did not impair the expansion of myeloid HO-1$^+$ cells in the BM (Fig. 6d,e). Furthermore, the number of blood F4/80$^+$CD88$^+$C3aR$^+$ cells expressing HO-1 was drastically reduced following treatment with anti-CSFR-1 or deletion of either NF-κB1 or C3 (Fig. 6f,g), indicating that this distinct myeloid subset catabolizes heme through HO-1 during emergency myelopoiesis instigated by pathological inflammation[34]. Consistently, anti-CSF1R treatment or NF-κB1 ablation in fibrosarcoma-bearing mice reduced levels of blood carboxyhemoglobin (COHb), a stable hemoglobin (Hb) complex acting as an indirect indicator of endogenous CO production[35] (Fig. 6h, left). In line with a systemic increase of COHb, tumor growth enhanced the expression of HO-1 also in spleen and liver macrophages (Fig. 6h right).

Furthermore, either condition conferred specific antitumor immunity to tumor lesions as evidenced by enhanced expression of IFNγ and GrzB in CD8$^+$ T cells, higher frequency of CD8$^+$CD44$^+$CD62L$^-$ effector memory cells and increased CD8$^+$/T$_{\mathrm{reg}}$ (CD4$^+$FoxP3$^+$) cell ratio (Fig. 6i). When HO-1-proficient mice were subcutaneously injected with 5×10^5 B16 cells and 3 days later treated with the HO-1 inhibitor ZnPPIX (Extended Data Fig. 6a–c), we observed reduced melanoma growth and reprogramming of myeloid and lymphoid functions, as also detected in B16-bearing *Hmox1*$^{\mathrm{fl/fl}}$*Lyz2-Cre* mice (Extended Data Fig. 4b–d). According, ex vivo treatment with ZnPPIX of FACS-sorted TAMs promoted a M2-to-M1 functional switch (Extended Data Fig. 6d). Analysis of HO-1 levels in TAMs and cancer cells, from both MN/MCA1 and B16 tumors, confirmed higher HO-1 levels in the F4/80$^{\mathrm{hi}}$ TAM population (Extended Data Fig 6e). In agreement, the antitumor activity of ZnPPIX treatment was lost in *Hmox1*$^{\mathrm{fl/fl}}$*Lyz2-Cre* B16-bearing mice (Extended Data Fig 6f, left). Of relevance, no differences were observed in the proliferation rate of MN/MCA1 and B16 cancer cells in response to ZnPPIX treatment (Extended Data Fig. 6f, right). The antimetastatic activity of ZnPPIX was confirmed in the metastatic melanoma model K1735-M2 (Extended Data Fig. 6g).

In support of the key role of CO in the polarization of TAMs, CORM-2 treatment of FACS-sorted TAMs reduced phosphorylation of the transcription factor STAT1 involved in M1 activation of macrophages while upregulating the phosphorylation of the M2-related transcription factors STAT6 and STAT3 (Extended Data Fig. 6h, top)[36]. According, TAMs treated ex vivo with CORM-2 upregulated the expression of typical M2-polarization markers (that is, CD206. CCL22, Arg1 and IL-10) and downregulated the expression of M1 markers (that is, TNF, CXCL10 and IL12p40) (Extended Data Fig. 6h, bottom).

Of note, depletion of CD4$^+$ and CD8$^+$ T lymphocytes in MN/MCA1 tumor-bearing mice reduced the antimetastatic activity of

Fig. 6 | Role of CSF1R in HO-1$^+$ TAM differentiation. **a**, Frequency of F4/80$^+$C3aR$^+$C5aR$^+$Ly6C$^{\mathrm{low/-}}$SiglecF$^-$ blood monocytes (left) and relative HO-1 expression (right) in WT naive and MN/MCA1 tumor-bearing mice. $n=7$ mice per group. **b**, Lethally irradiated CD45.2$^+$ mice were grafted with syngeneic BM CD45.1$^+$ cells and, after 8 weeks, injected with MN/MCA1 tumor cells. Left, level of chimerism (percentage of CD45.1$^+$ and CD45.2$^+$ cells) within blood and tumor-infiltrated leukocytes (percentage of CD45$^+$ cells). Middle, HO-1 expression by CD45.2$^+$ and CD45.1$^+$ F4/80$^{\mathrm{hi}}$ TAMs. Right, CCR2 expression in HO-1$^{\mathrm{hi}}$ and HO-1$^{\mathrm{lo/-}}$ F4/80$^{\mathrm{hi}}$ TAMs. $n=5$ mice per group. **c**, Left, percentage of CMPs (CD16/32$^-$CD34$^+$ cells), MEPs (CD16/32$^-$CD34$^-$ cells) and GMPs (CD16/32$^+$CD34$^+$ cells). Right, HO-1 expression in BM of WT naive and MN/MCA1 tumor-bearing mice. $n=3$ or 4 mice per group. **d**, Percentage of CMPs, MEPs and GMPs and relative HO-1 expression in BM of untreated and anti-CSF1R-treated melanoma-bearing WT mice (top) and of WT, *p50*$^{-/-}$ and *C3*$^{-/-}$ fibrosarcoma-bearing mice (bottom). $n=4$–6 mice per group. **e**, Percentage of Gr1$^-$CD11b$^+$F4/80$^+$ cells (left, second from right) and relative HO-1 expression (right, second from left) in BM of untreated and anti-CSF1R-treated melanoma-bearing WT mice (left, second from left) and of WT, *p50*$^{-/-}$ and *C3*$^{-/-}$ fibrosarcoma-bearing mice (right, second from right). Right, $n=4$ or 8 (WT) and $n=4$–5 (*p50*$^{-/-}$ and *C3*$^{-/-}$) mice. Left, $n=4$ (tumor-free), $n=10$ (vehicle) and $n=6$ (anti-CSF1R) mice. **f**, F4/80$^+$C3aR$^+$C5aR$^+$Ly6C$^{\mathrm{low/-}}$SiglecF$^-$ monocyte frequency (left) and relative HO-1 expression (right) in blood of untreated and anti-CSF1R-treated B16-bearing WT mice. $n=5$–6 mice per group. **g**, Frequency of F4/80$^+$C3aR$^+$C5aR$^+$Ly6C$^{\mathrm{low/-}}$SiglecF$^-$ monocytes (left, second from right) and relative HO-1 expression (right, second from left) in blood of untreated and anti-CSF1R-treated fibrosarcoma-bearing WT and *p50*$^{-/-}$ fibrosarcoma-bearing mice and of WT and *C3*$^{-/-}$ sarcoma-bearing mice. Left, $n=2$ (tumor-free), $n=4$–5 (vehicle and anti-CSF1R) mice. Right, $n=4$–5 mice per group. **h**, Effects of anti-CSF1R on blood levels of COHb in WT and *p50*$^{-/-}$ MN/MCA1-bearing mice (left) and of HO-1 in splenic and liver macrophages in tumor-free and tumor-bearing WT mice (right). Left, $n=5$ (WT) and $n=6$ (*p50*$^{-/-}$) mice. Right, $n=4$–5 mice per group. **i**, IFN-γ$^+$ and GrzB$^+$ in CD8$^+$ T and effector memory CD8$^+$ T cells and the CD8$^+$/T$_{\mathrm{reg}}$ ratio in WT and *p50*$^{-/-}$ MN/MCA1-bearing mice, treated or not with anti-CSF1R. $n=4$ mice per group. **j**, Tumor volume and lung metastatic area in T-lymphocyte-depleted (anti-CD4/CD8) MN/MCA1-bearing WT mice, treated or not with ZnPPIX (HO-1 antagonist); the area of metastatic burden was quantified from H&E-stained lung sections from the same sample and is expressed as a percentage of total lung surface area. Representative images are shown. Scale bars, 1 mm. Left, $n=5$ (vehicle and ZnPPIX) and $n=6$ (anti-CD4/CD8 + ZnPPIX) mice. Right, $n=3$ (vehicle and ZnPPIX) and $n=6$ (anti-CD4/CD8 + ZnPPIX) mice. **k**, MN/MCA1 growth and metastatic area in *Hmox1*$^{\mathrm{fl/fl}}$ and *Hmox1*$^{\mathrm{fl/fl}}$*Lyz2-Cre* mice, treated or not with anti-PD-1 antibody; the area of metastatic burden was quantified from H&E-stained lung sections from the same sample and is expressed as a percentage of total lung surface area. Representative images are shown. Scale bars, 1 mm. $n=8$ (*Hmox1*$^{\mathrm{fl/fl}}$ vehicle, *Hmox1*$^{\mathrm{fl/fl}}$ + anti-PD-1) and $n=7$ (*Hmox1*$^{\mathrm{fl/fl}}$*Lyz2-Cre* vehicle and *Hmox1*$^{\mathrm{fl/fl}}$*Lyz2-Cre* + anti-PD-1) mice. **a**, Data are representative of two independent experiments. **b**–**k**, One experiment was performed. Data are mean ± s.e.m. NS, not significant. $^*P<0.05$, $^{**}P<0.01$, $^{***}P<0.001$, $^{****}P<0.0001$ between selected relevant comparisons. **a**–**g**, One-way ANOVA or two-tailed unpaired Student's *t*-test. **h**–**j**, Two-way ANOVA with Šidák's multiple comparisons test. **k**, One-way ANOVA followed by Tukey's multiple comparison test.

ZnPPIX (Fig. 6j), confirming the immunosuppressive effects of HO-1-driven heme catabolism. Further, while ZnPPIX treatment inhibited the frequency of CD31$^+$ cells in primary tumors, as well as EMT activity, both events were reversed by CD4$^+$/CD8$^+$ T-cell depletion (Extended Data Fig. 6i). In good agreement with a protumorigenic role of HO-1$^+$ TAMs, myeloid-specific ablation of HO-1

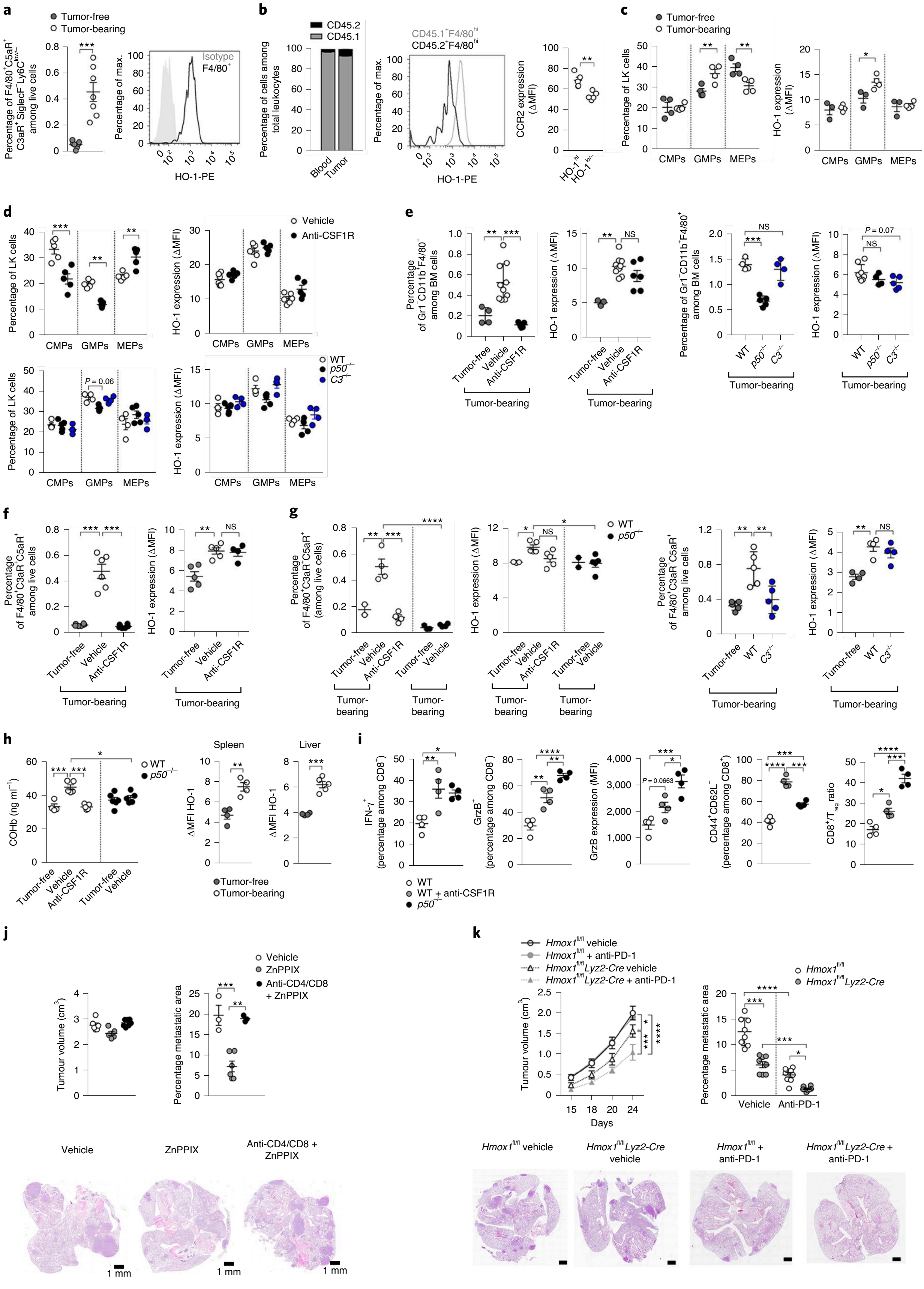

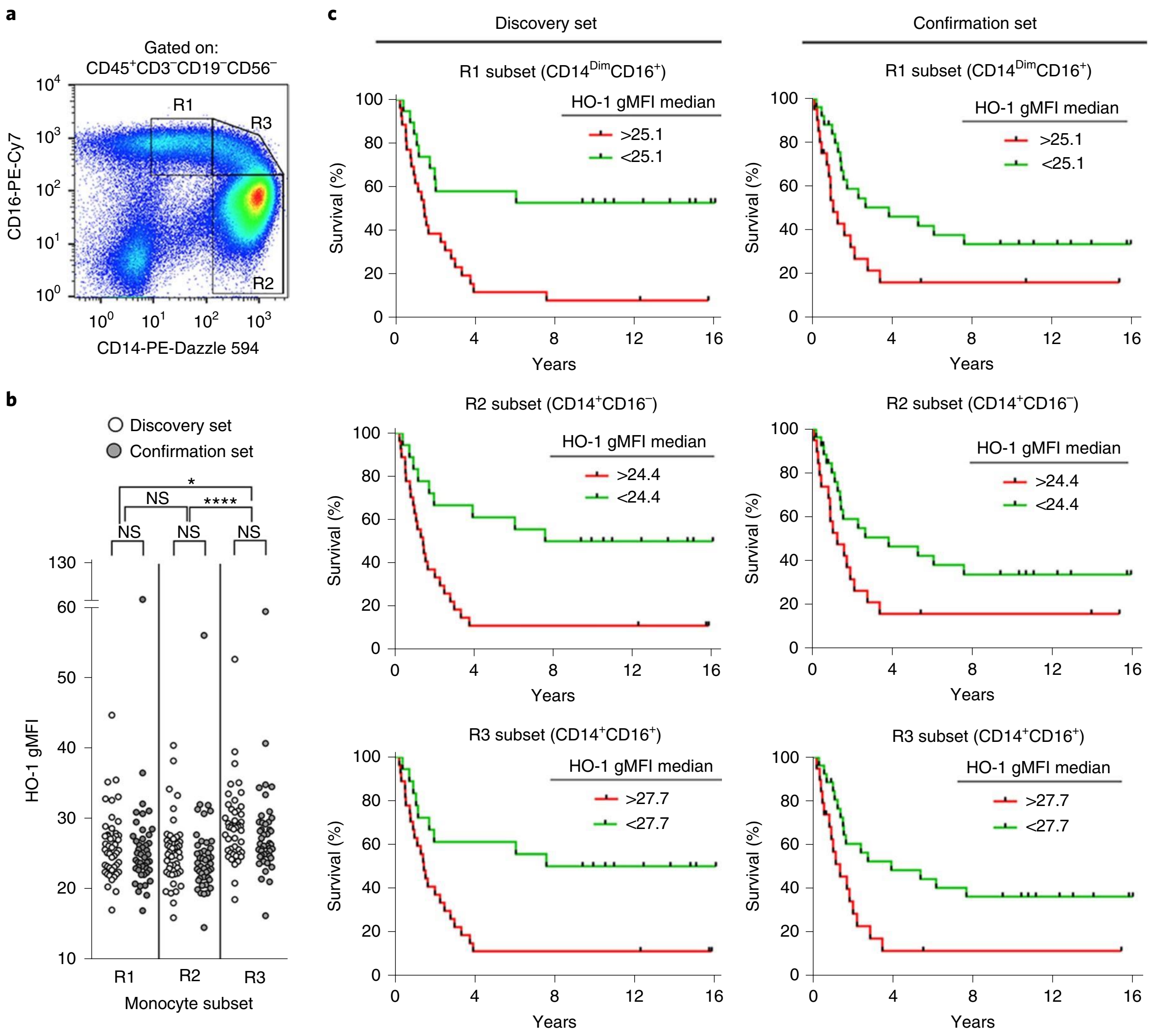

Fig. 7 | Prognostic significance of myeloid-specific HO-1. a, Gating strategy to identify three key blood monocyte subsets (R1–R3) in patients with melanoma. **b**, Expression of HO-1 (gMFI) in subsets R1–R3 from the discovery and confirmation sets of patients with AJCC stage IIIC/IV melanoma. **c**, Kaplan–Meier survival analysis in discovery (left) and confirmation sets (right) stratified by monocyte subset-specific HO-1 gMFI median value of the combined set (discovery + confirmation). **b**,**c**, $n = 47$ (discovery set) and $n = 45$ (confirmation set) patients. Data are mean ± s.e.m. NS, not significant. $^*P < 0.05$, $^{****}P < 0.0001$ between selected relevant comparisons using Mann–Whitney *U*-test.

in MN/MCA1 fibrosarcoma (Fig. 6k) or ZnPPIX cotreatment of B16 melanoma (Extended Data Fig. 6j) improved the antitumor efficacy of an anti-PD-1 monoclonal antibody[37]. Thus, C3 and M-CSF activities converge on Nrf2 activation in a p50-dependent manner, promoting the expansion of BM-derived HO-1$^+$ TAMs that fuel CO-mediated M2 polarization and inhibit antitumor immunity.

Prognostic significance of myeloid-specific HO-1 in melanoma patients. Since our results indicated that the accumulation of proangiogenic and prometastatic HO-1$^+$ TAMs is consistent with the increased number of HO-1$^+$ blood monocytes observed in tumor bearers, we assessed the potential prognostic significance of HO-1 expression in 15 blood monocyte subsets (R1–R3 and R1R5–R3R8) (Extended Data Fig. 7a) of two consecutive cohorts of patients with American Joint Committee on Cancer (AJCC) stage IIIC/IV melanoma (discovery cohort: $n = 47$; confirmation cohort: $n = 45$) (Supplementary Table 2 and Extended Data Fig. 7b,c). Semiparametric Cox regression analyses revealed a significant association of HO-1 expression values (geometric mean of fluorescence intensity, gMFI) with survival in both patient cohorts (Fig. 7a–c, Extended Data Fig. 8a,b and Supplementary Table 3a,c).

To establish a clinical and phenotypic connection between peripheral blood and the tumor microenvironment, we first performed immunohistochemistry on a panel of metastatic lesions from patients with stage III melanoma, to test for HO-1 expression. HO-1 staining was observed in the same stromal or intratumor areas positive also for the M2 marker CD163 (Extended Data Fig. 9a, patient nos. 1–8). Lesions lacking HO-1 were also negative for CD163 (Extended Data Fig. 9a, patient nos. 11–15). In this small panel of lesions, HO-1 expression was observed in patients with shorter survival compared with HO-1-negative cases (Extended Data Fig. 9a). Moreover, by using the survival module of the TIMER2.0 web resource for analysis of immune infiltrates across diverse cancer types, we tested the potential prognostic significance of both HMOX1 gene expression and macrophage gene-signature M2_TIDE in The Cancer Genome Atlas (TCGA) melanoma dataset. In addition to clinical stage, both M2_TIDE gene signature and HMOX1 gene expression were significant in a Cox proportional hazards model (Extended Data Fig. 9b) while two macrophage-related genes (CD163 and CD68) were not. Together with our preclinical evidences, these results confirm that tumors induced expansion of blood monocytes and TAMs expressing HO-1, establishing correlation of their increased frequency with a negative prognosis.

Discussion

Tumors promote a pathological expansion of myeloid populations, whose specialized heterogeneity differentially affects disease progression[34,38]. Deciphering the molecular basis of such heterogeneity remains a great challenge that is expected to reveal therapeutic opportunities through restoration of anticancer functions. Our findings add to the complexity of TAM specialization[39] by identifying the pathways involved in differentiation (M-CSF) and recruitment (M-CSF and C3a) of distinct BM-derived, prometastatic HO-1$^+$ TAMs. We provide evidence that, in response to immunological stresses such as those promoted by bacterial products and growing tumors, a distinct HO-1-expressing monocyte/macrophage population emerges from BM precursors. Phenotypically, HO-1$^+$ TAMs resemble the erythrophagocytic macrophages present in the red pulp of the spleen and, to some extent, those in the liver, which play a crucial role in iron metabolism and are specialized in heme biosynthesis originating from senescent red blood cells[40]. In cancer this population accumulates in blood and at the invasive tumor margin under the influence of the p50 NF-κB–CSF-R1–C3aR axis, which converges on Nrf2 activation to support HO-1 expression by TAMs.

This finding offers a new example of cooptation of physiological functions used by tumors. Thus, while HO-1 catabolism has homeostatic properties offering protection against a variety of immune-mediated inflammatory diseases[41], our findings indicate that tumors exploit HO-1 activity by myeloid cells to promote immunosuppression, angiogenesis and EMT, enhancing metastasis formation. Importantly, HO-1$^+$ TAMs appear to be a druggable target since pharmacological inhibition or myeloid-specific ablation of HO-1 prevented these protumor events while increasing specific antitumor immunity and the efficacy of anti-PD-1-mediated immunotherapy. In agreement, similar antitumor effects were obtained through inhibition of recruiting pathways of HO-1$^+$ TAMs (that is, M-CSF or C3a). The clinical relevance of the HO-1$^+$ myeloid population was demonstrated both by immunohistochemical investigation of metastatic lesions from patients with stage III melanoma and by evaluation of the prognostic significance of the HMOX1 gene in the TCGA melanoma dataset. Furthermore, correlation of blood levels of HO-1$^+$ myeloid cells in patients with stage III/IV melanoma correlated this population with a worse survival, identifying this population also as a prognostic blood marker. Interestingly, HO-1$^+$ TAMs express high levels of SIGLEC1 and CCL8 genes, two markers of poor prognosis recently identified in a distinct TAM subgroup found in patients with breast cancer[23]. Based on the crucial role of CO in protumoral TAM M2 polarization, and the possibility of modulation of blood COHb levels through HO-1$^+$ myeloid cell depletion, our study also suggests a thorough review of the impact of cigarette smoking on prognosis and therapeutic response in cancer patients.

Online content

Any methods, additional references, Nature Research reporting summaries, source data, extended data, supplementary information, acknowledgements, peer review information; details of author contributions and competing interests; and statements of data and code availability are available at https://doi.org/10.1038/s41590-021-00921-5.

Received: 27 January 2020; Accepted: 19 March 2021;
Published online: 26 April 2021

References

1. Ueha, S., Shand, F. H. & Matsushima, K. Myeloid cell population dynamics in healthy and tumor-bearing mice. *Int. Immunopharmacol.* **11**, 783–788 (2011).
2. Yang, M., McKay, D., Pollard, J. W. & Lewis, C. E. Diverse functions of macrophages in different tumor microenvironments. *Cancer Res.* **78**, 5492–5503 (2018).
3. Gordon, S. & Pluddemann, A. The mononuclear phagocytic system. Generation of diversity. *Front. Immunol.* **10**, 1893 (2019).
4. Strauss, L. et al. RORC1 regulates tumor-promoting 'emergency' granulo-monocytopoiesis. *Cancer Cell* **28**, 253–269 (2015).
5. Mantovani, A., Allavena, P., Sica, A. & Balkwill, F. Cancer-related inflammation. *Nature* **454**, 436–444 (2008).
6. Mantovani, A., Marchesi, F., Malesci, A., Laghi, L. & Allavena, P. Tumour-associated macrophages as treatment targets in oncology. *Nat. Rev. Clin. Oncol.* **14**, 399–416 (2017).
7. Sica, A., Guarneri, V. & Gennari, A. Myelopoiesis, metabolism and therapy: a crucial crossroads in cancer progression. *Cell Stress* **3**, 284–294 (2019).
8. Mehla, K. & Singh, P. K. Metabolic regulation of macrophage polarization in cancer. *Trends Cancer* **5**, 822–834 (2019).
9. Blagih, J. & Jones, R. G. Polarizing macrophages through reprogramming of glucose metabolism. *Cell Metab.* **15**, 793–795 (2012).
10. Wang, D., Paz-Priel, I. & Friedman, A. D. NF-κB p50 regulates C/EBPα expression and inflammatory cytokine-induced neutrophil production. *J. Immunol.* **182**, 5757–5762 (2009).
11. Porta, C. et al. Protumor steering of cancer inflammation by p50 NF-κB enhances colorectal cancer progression. *Cancer Immunol. Res.* **6**, 578–593 (2018).
12. Ziegler-Heitbrock, L. The p50-homodimer mechanism in tolerance to LPS. *J. Endotoxin Res.* **7**, 219–222 (2001).
13. Porta, C. et al. Tolerance and M2 (alternative) macrophage polarization are related processes orchestrated by p50 nuclear factor κB. *Proc. Natl Acad. Sci. USA* **106**, 14978–14983 (2009).
14. Gozzelino, R., Jeney, V. & Soares, M. P. Mechanisms of cell protection by heme oxygenase-1. *Annu. Rev. Pharmacol. Toxicol.* **50**, 323–354 (2010).
15. Sica, A. et al. Bacterial lipopolysaccharide rapidly inhibits expression of C-C chemokine receptors in human monocytes. *J. Exp. Med.* **185**, 969–974 (1997).
16. Reis, E. S., Mastellos, D. C., Ricklin, D., Mantovani, A. & Lambris, J. D. Complement in cancer: untangling an intricate relationship. *Nat. Rev. Immunol.* **18**, 5–18 (2018).
17. Schraufstatter, I. U., Discipio, R. G., Zhao, M. & Khaldoyanidi, S. K. C3a and C5a are chemotactic factors for human mesenchymal stem cells, which cause prolonged ERK1/2 phosphorylation. *J. Immunol.* **182**, 3827–3836 (2009).
18. De Palma, M. et al. Tie2 identifies a hematopoietic lineage of proangiogenic monocytes required for tumor vessel formation and a mesenchymal population of pericyte progenitors. *Cancer Cell* **8**, 211–226 (2005).
19. Jenkins, S. J. & Hume, D. A. Homeostasis in the mononuclear phagocyte system. *Trends Immunol.* **35**, 358–367 (2014).
20. Saccani, A. et al. p50 nuclear factor-κB overexpression in tumor-associated macrophages inhibits M1 inflammatory responses and antitumor resistance. *Cancer Res.* **66**, 11432–11440 (2006).
21. Vadrevu, S. K. et al. Complement c5a receptor facilitates cancer metastasis by altering T-cell responses in the metastatic niche. *Cancer Res.* **74**, 3454–3465 (2014).
22. Markiewski, M. M. et al. Modulation of the antitumor immune response by complement. *Nat. Immunol.* **9**, 1225–1235 (2008).
23. Cassetta, L. et al. Human tumor-associated macrophage and monocyte transcriptional landscapes reveal cancer-specific reprogramming, biomarkers, and therapeutic targets. *Cancer Cell* **35**, 588–602 (2019).
24. Gozzelino, R. & Soares, M. P. Coupling heme and iron metabolism via ferritin H chain. *Antioxid. Redox Signal.* **20**, 1754–1769 (2014).
25. Otterbein, L. E. et al. Carbon monoxide has anti-inflammatory effects involving the mitogen-activated protein kinase pathway. *Nat. Med.* **6**, 422–428 (2000).
26. Nitti, M. et al. HO-1 induction in cancer progression: a matter of cell adaptation. *Antioxididants (Basel)* **6**, 29 (2017).
27. Weis, N., Weigert, A., von Knethen, A. & Brune, B. Heme oxygenase-1 contributes to an alternative macrophage activation profile induced by apoptotic cell supernatants. *Mol. Biol. Cell* **20**, 1280–1288 (2009).
28. Ponka, P. Tissue-specific regulation of iron metabolism and heme synthesis: distinct control mechanisms in erythroid cells. *Blood* **89**, 1–25 (1997).
29. Park, J. Y. et al. Polarized CD163$^+$ tumor-associated macrophages are associated with increased angiogenesis and CXCL12 expression in gastric cancer. *Clin. Res. Hepatol. Gastroenterol.* **40**, 357–365 (2016).
30. Brouard, S. et al. Heme oxygenase-1-derived carbon monoxide requires the activation of transcription factor NF-κB to protect endothelial cells from tumor necrosis factor-α-mediated apoptosis. *J. Biol. Chem.* **277**, 17950–17961 (2002).

31. Zhou, C. et al. The heme oxygenase-1 inhibitor ZnPPIX induces non-canonical, Beclin 1-independent, autophagy through p38 MAPK pathway. *Acta Biochim. Biophys. Sin. (Shanghai)* **44**, 815–822 (2012).
32. Sun, J. et al. Hemoprotein Bach1 regulates enhancer availability of heme oxygenase-1 gene. *EMBO J.* **21**, 5216–5224 (2002).
33. Ren, D. et al. Brusatol enhances the efficacy of chemotherapy by inhibiting the Nrf2-mediated defense mechanism. *Proc. Natl Acad. Sci. USA* **108**, 1433–1438 (2011).
34. Gabrilovich, D. I., Ostrand-Rosenberg, S. & Bronte, V. Coordinated regulation of myeloid cells by tumours. *Nat. Rev. Immunol.* **12**, 253–268 (2012).
35. McArdle, A. J. et al. Determinants of carboxyhemoglobin levels and relationship with sepsis in a retrospective cohort of preterm neonates. *PLoS ONE* **11**, e0161784 (2016).
36. Sica, A. & Mantovani, A. Macrophage plasticity and polarization: in vivo veritas. *J. Clin. Invest.* **122**, 787–795 (2012).
37. Ribas, A. Tumor immunotherapy directed at PD-1. *N. Engl. J. Med.* **366**, 2517–2519 (2012).
38. Wu, W. C. et al. Circulating hematopoietic stem and progenitor cells are myeloid-biased in cancer patients. *Proc. Natl Acad. Sci. USA* **111**, 4221–4226 (2014).
39. Hoeffel, G. & Ginhoux, F. Fetal monocytes and the origins of tissue-resident macrophages. *Cell. Immunol.* **330**, 5–15 (2018).
40. Korolnek, T. & Hamza, I. Macrophages and iron trafficking at the birth and death of red cells. *Blood* **125**, 2893–2897 (2015).
41. Soares, M. P. & Bach, F. H. Heme oxygenase-1: from biology to therapeutic potential. *Trends Mol. Med.* **15**, 50–58 (2009).

Publisher's note Springer Nature remains neutral with regard to jurisdictional claims in published maps and institutional affiliations.

© The Author(s), under exclusive licence to Springer Nature America, Inc. 2021

Methods

Animals. All mice used in this study were 8–12 weeks of age, and both males and females were used. Individual experiments were age and sex matched. Wild-type C57BL6/J and C3H/HeN mice were obtained from Charles River Laboratories. NF-κB1/p50-deficient mice were available in-house[20]. Homozygous *C3* mutant mice (B6;129S4-*C3*^{tm1Crr}/J) were purchased from Jackson Laboratories. NFKB1$^{flox/flox}$ (*p50*$^{fl/fl}$) mice were recently generated in our laboratory[11]. *p50*$^{fl/fl}$ mice were crossed with B6.129P2-Lyz2tm1(cre)Ifo/J mice (Jackson Laboratories) to generate *p50*$^{fl/fl}$*Lyz2-Cre* mice. *Hmox1*$^{fl/fl}$ and *Hmox1*$^{fl/fl}$*Lyz2-Cre* mice[42] were kindly provided by B. Wegiel (Beth Israel Deaconess Medical Center, Harvard Medical School, Boston, USA). All colonies were housed and bred in the specific-pathogen-free animal facility at the Humanitas Clinical and Research Center (Rozzano, Milan, Italy) in individually ventilated cages. Mice were housed under a 12/12-h light/dark cycle at an ambient temperature of 22 ± 1 °C with humidity 52–55%. Mice were randomized based on sex, age and weight. All procedures involving handling and care of C57BL/6J mice complied with protocols approved by the Humanitas Clinical and Research Center and in accordance with national (Legislative Decree no. 116, G.U., suppl. 40, 02-18-1992 and no. 26, G.U., 03-04-2014) and international law and policies (EEC, Council Directive nos. 2010/63/EU, OJ L 276/33 and 09-22-2010; National Institutes of Health Guide for the Care and Use of Laboratory Animals, US National Research Council, 2011). The study was approved by the Italian Ministry of Health (nos. 97/2014-PR and 25/2018-PR). All efforts were made to minimize the number of animals used and their suffering.

Cells. The following mycoplasma-free cell lines were used: 3-MCA-derived sarcoma cell line MN/MCA1 and melanoma cells B16/F10 and K1735-M2. B16/F10 cells were purchased from ATCC; K1735-M2 cells were kindly provided by L. Carminati (Laboratory of Tumor Microenvironment, Istituto di Ricerche Farmacologiche Mario Negri IRCCS, Bergamo, Italy). The 3-MCA-derived sarcoma cell line MN/MCA1 was derived from stock periodically renewed through primary cells isolated from tumors implanted in WT mice. All cell lines were mycoplasma-free. Nfr2$^{-/-}$ BM cells derived from *Nfe2l2*$^{-/-}$ mice were available from M. P. Soares (Inflammation Laboratory, Instituto Gulbenkian de Ciência, Oeiras, Portugal)[43].

Cancer models. Mice were injected intramuscularly in their left hindlimb with 3-MCA-derived, mycoplasma-free sarcoma cell line MN/MCA1 (10^5 or 10^4 cells per mouse in 100 μl of PBS). From day 14 after tumor cell injection, primary tumor growth was monitored three times per week with a caliper. Mice were subcutaneously injected with 100 μl of PBS containing 5×10^5 murine melanoma B16/F10 cells. Ten days after tumor cell injection, tumor growth was monitored three times per week with a caliper. For spontaneous lung metastasis assay, mice were subcutaneously injected with 100 μl of PBS containing 5×10^5 murine melanoma B16/F10 cells. Growth of the primary tumor was monitored with a caliper and, when tumors reached 0.8–1.0 cm^3, mice were anesthetized and tumors surgically removed; for analysis of spontaneous lung metastasis, all mice were autopsied 30 days after surgery. Melanoma K1735-M2 (10^5 cells per mouse) were implanted subcutaneously in the flank of C3H/HeN mice. Growth of the primary tumor was monitored with a caliper and, when tumors reached 800–1,000 mm^3, mice were anesthetized and tumors surgically removed; for analysis of spontaneous lung metastasis, all mice were autopsied 30 days after surgery. *Hmox1*$^{fl/fl}$ and *Hmox1*$^{fl/fl}$*Lyz2-Cre* mice were injected intramuscularly in the left hindlimb with MN/MCA1 mCherry$^+$ (10^5 cells per mouse in 100 μl of PBS); blood was collected 20 days after tumor cell injection and analyzed by RT–PCR for mCherry expression and by FACS for circulating MN/MCA1 mCherry$^+$ tumor cell quantification.

In vivo treatments. From day 10 after tumor cell injection, MN/MCA1-bearing mice were treated intraperitoneally with a CSF1R antagonist (a kind gift from C. Ries, Roche Diagnostic, Penzberg, Germany) at an initial dose of 60 mg kg^{-1}, followed by twice-weekly doses of 30 mg kg^{-1} for the duration of the experiment. Control mice were injected with an isotype antibody. From day 7 post implantation, MN/MCA1-bearing mice were intraperitoneally injected with 30 mg kg^{-1} ZnPPIX (Frontier Scientific) three times per week. When specified, starting from the day before tumor injection, mice received an intraperitoneal injection of 0.3 mg of anti-mouse CD4 (Rat Anti-Mouse CD4 Monoclonal Antibody, Unconjugated, Clone GK1.5, BioXcell) and 0.3 mg of anti-mouse CD8 (Rat Anti-Mouse CD8α Monoclonal Antibody, Unconjugated, Clone 2.43, BioXcell) once per week for the duration of the experiment. FACS analysis of peripheral blood samples confirmed depletion of CD4$^+$ and CD8$^+$ cells over 7 days. B16-bearing mice were intraperitoneally injected with 30 mg kg^{-1} ZnPPIX (Frontier Scientific) from day 3 post implantation, three times per week, either separately or in combination with 100 μg of anti-PD-1 antibody (Clone RPM1-14, BioXcell), twice per week, starting 9 days after tumor cell injection. For the spontaneous metastasis assay, ZnPPIX (30 mg kg^{-1}, intraperitoneally, 2 days per week) was given before and after surgical removal of K1735-M2 primary melanomas[44], performed when tumors had reached a mean volume of 1 cm^3; all mice were autopsied 30 days postoperatively. To induce LPS tolerance in vivo, 8-week-old WT and *p50*$^{-/-}$ mice, weighing approximately 20 g, were injected intraperitoneally with 200 μg of LPS (from *Escherichia coli* strain B05.55; Sigma). Blood was collected 0, 6 and 24 h following LPS injection for flow cytometry analysis. From day 7 after tumor cell injection, MN/MCA1-bearing mice were treated intraperitoneally with 2 mg kg^{-1} brusatol (Sigma, catalog no. SML1868), three times per week for the duration of the experiment.

Lung histology. Lungs were collected following intracardiac perfusion with cold PBS and were formalin fixed for 24 h, dehydrated and paraffin embedded for histologic analysis. Histology was performed on longitudinal serial sections (100 μm apart, width 8 μm) from each lung, stained with hematoxylin and eosin (H&E) and scanned using a VS120 Dot-Slide BX61 virtual slide microscope (Olympus Optical). The area of lung lesions was obtained by manual tracing of the perimeter of lesions using Image Pro-Premiere software 9.2 (Media Cybernetics).

Adoptive transfer experiments. FACS-sorted F4/80^{hi}C5aR1^{hi} and F4/80^{lo}C5aR1^{lo} TAMs (2×10^5) from WT MN/MCA1 sarcomas were injected intramuscularly, together with 10^5 MN/MCA1 tumor cells, into the hindlimb of WT or *p50*$^{-/-}$ mice. After sacrifice, lungs were fixed and macroscopic metastases enumerated.

Generation of BM chimeras. CD45.2 WT mice were lethally irradiated with a total dose of 900 cGy. Two hours later, mice were injected in the retro-orbital plexus with 5×10^6 nucleated BM cells, isolated by flushing the cavity of a freshly dissected femur from CD45.1 WT donors. Ten days before irradiation, recipient mice received gentamycin (0.8 mg ml^{-1} in drinking water), which was administered for an additional 2 weeks. BM reconstitution was evaluated 6 weeks after transplantation by flow cytometry of peripheral blood and was deemed positive if >90%. Eight weeks after BM transplantation, mice were injected with MN/MCA1 tumor cells.

Patients. Human peripheral blood leukocytes were isolated from two consecutive cohorts (discovery and confirmation) of stage IIIC/IV (AJCC melanoma staging system, eighth edition), undergoing surgical treatment for metastatic melanoma at the Fondazione IRCCS Istituto Nazionale dei Tumori, Milan, Italy between November 2001 and September 2003. Samples from the cohorts described in this study were obtained based on informed consent. The study was conducted according to the Declaration of Helsinki Principles and following approval by the Ethics Committee of Fondazione IRCCS, Istituto Nazionale dei Tumori, Milan, Italy. The main clinical parameters, including type of therapy after isolation of peripheral blood lymphocytes of all patients, are listed in Supplementary Table 2. The discovery set ($n = 47$) included patients in AJCC stages IIIC ($n = 35$) and IV ($n = 12$). The confirmation set ($n = 45$) included patients in AJCC stages IIIC ($n = 31$) and IV ($n = 14$).

FACS analysis of human samples. Human peripheral mononuclear cells were obtained by Ficoll density gradient centrifugation (Ficoll-Paque PLUS, GE Healthcare). Multicolor staining for cell populations was performed on cryopreserved samples. Cells were thawed in RPMI medium supplemented with 10% human serum; 2×10^6 lymphocytes were resuspended in 100 μl of staining buffer (PBS + 2% fetal bovine serum (FBS)) and incubated with FcR Blocking Reagent (Miltenyi Biotec) with antibodies against the indicated cell surface markers and Zombie Aqua (Fixable viability dye, Biolegend) in staining buffer for 30 min at 4 °C. The following human antibodies were used: CD14-PE-CF594 (M5E2) (1/200, Biolegend catalog no. 301851, CD3-PerCP-Cy5.5 (UCHT1) (1/100, Biolegend catalog no. 300430), CD16-PE-Cy7 (3G8) (1/400, Biolegend catalog no. 302015), CD45-BV421 (HI30) (1/200, Biolegend catalog no. 304032), CD88-PE (S5/1) (1/200, Biolegend catalog no. 344303), CD19-PerCP-Cy5.5 (SJ25C1) (1/100, Biolegend catalog no. 363015), CD56-PerCP-Cy5.5 (5.1H11) (1/100, Biolegend catalog no. 362505), Tie2/CD202b-Alexa Fluor 647 (33.1) (1/200, Biolegend catalog no. 334209) and HMOX1 FITC (1/200, Abcam catalog no. ab69545).

Cell permeabilization was obtained with a Cytofix/Cytoperm Fixation/Permeabilization Solution Kit (BD Pharmingen) according to the manufacturer's instructions. After permeabilization, cells were stained with HO-1 mAb (FITC, Abcam catalog. no. ab69545) for 30 min at 4 °C and acquired by a ten-color Gallios (Beckman Coulter) cytometer. Instrument optical alignment and fluidics were routinely checked by Flow-Check Fluorospheres (Beckman Coulter), while Flow-Set Fluorospheres (Beckman Coulter) were used for control of light scatter and fluorescence intensity. Data were analyzed with FlowJo software (v.10.5.3, FlowJo, LLC) after exclusion of doublets (on SSC-A versus SSC-H dot plots) and by gating on live (Zombie Aqua-) cells. Fifteen monocyte subsets were identified by staining for CD14, CD16, CD88 and Tie2 (subsets R1–R3 and R1R5–R3R8) with the gating strategy shown in Extended Data Fig. 7a. All subsets expressed intracellular HO-1, recorded as gMFI in permeabilized cells (Extended Data Fig. 7b). The distribution of HO-1 gMFI values for all monocyte subsets, in both discovery and confirmation cohorts, did not pass the D'Agostino–Pearson Normality test (alpha = 0.05; Supplementary Table 2b). Within each monocyte subset, HO-1 gMFI values showed no significant differences when comparing discovery and confirmation cohorts (Mann–Whitney test; Supplementary Table 2c). However, distinct monocyte subsets showed significant differences in the combined set of gMFI HO-1 values (Kruskal–Wallis test followed by Dunn's multiple comparison test; Extended Data Fig. 7c).

FACS analysis of murine samples. Primary tumors were cut into small pieces, disaggregated with 0.5 mg ml^{-1} COL IV and 150 U ml^{-1} DNase I in RPMI 1640 for 30 min at 37 °C and filtered through strainers. Macroscopic lung metastatic lesions were removed with tweezers. Pulmonary nodules isolated were finely minced, disaggregated with 0.5 mg ml^{-1} COL IV and 150 U ml^{-1} DNase I in RPMI 1640 for 30 min at 37 °C and filtered through Falcon strainers (70 µm). Splenocytes were collected from spleens after disaggregation and filtration through Falcon strainers (70 µm). Livers were removed, cut into small pieces and gently mashed through a cell strainer (70 µm) followed by enrichment of the leukocyte population on a 35% Percoll gradient (Sigma). BM cells were isolated from the tibias and femurs of both tumor-free and tumor-bearing mice. Whole blood samples were collected from the facial vein or heart in EDTA-coated collection tubes and directly processed using a standardized red blood cell lysis protocol. Cells were resuspended in Hank's balanced salt solution (Lonza) supplemented with 0.5% bovine serum albumin (BSA) (Sigma-Aldrich). Staining was performed at 4 °C for 20 min with the following mouse antibodies:

CD45-FITC (30-F11) (1/400, Biolegend catalog no. 103108); CD45-PerCP (30-F11) (1/200, Biolegend catalog no. 103130); CD45-BUV563 (30-F11) (1/400, BD Horizon catalog no. 565710); CD45.1-APC (A20) (1/200, Biolegend catalog no. 110714); CD45.2-FITC (104) (1/200, Biolegend catalog no. 109806); CD11b-PerCp-Cy5.5 (M1/70) (1/200, eBioscience catalog no. 45-0112-82); CD11b-PE (M1/70) (1/400, Biolegend catalog no. 101208); CD11b-FITC (M1/70) (1/200, Biolegend catalog no. 101206); CD11b-BV711 (M1/70) (1/600, Biolegend catalog no. 101242); F4/80-APC (BM8) (1/100, Biolegend catalog no. 123116); F4/80-PE (BM8) (1/200, Biolegend catalog no. 123110); F4/80-PE-Cy7 (BM8) (1/200, Biolegend catalog no. 123114); F4/80-BV421 (BM8) (1/100, Biolegend catalog no. 123137); Ly6G-PE (1A8) (1/200, Biolegend catalog no. 127608); Ly6G-BV570 (1A8) (1/100, Biolegend catalog no. 127629); Ly6C- APC-Cy7 (HK1.4) (1/600, eBioscience catalog no. 47-5932-82); MHCII-PE-Cy7 (M5/114.15.2) (1/200, eBioscence catalog no. 78-5321-82); MHCII-PE (M5/114.15.2) (1/400, Biolegend catalog no. 107607); MHCII-BV480 (M5/114.15.2) (1/600, BD Horizon catalog no. 566088); CD11c-APC (N418) (1/100, Biolegend catalog no. 117310); CD11c-BV605 (N418) (1/200, eBioscence catalog no. 63-0114-82); CD8-APC (53-6.7) (1/100, Biolegend catalog no. 100712); CD8-BUV805 (53-6.7) (1/200, BD Horizon catalog no. 564920); CD4-PE (GK1.5) (1/200, Biolegend catalog no. 100408); CD4-PE-Cy7 (GK1.5) (1/200, Biolegend catalog no. 100422); CD4-BUV496 (GK1.5) (1/100, BD Horizon catalog no. 564667); CD3-PerCP (145-2C11) (1/100, Biolegend catalog no. 100326); CD3-BV650 (145-2C11) (1/100, Biolegend catalog no. 100229); IFNγ-FITC (XMG1.2) (1/100, Biolegend catalog no. 505806); IFNγ-PE (XMG1.2) (1/200, BD Pharmingen catalog no. 554412); FoxP3-Alexa Fluor 488 (MF23) (1/100, BD Pharmingen catalog no. 560403); FoxP3-Alexa Fluor 647 (MF23) (1/100, BD Pharmingen catalog no. 560402); CD115-PE (AFS98) (1/100, Biolegend catalog no. 135505); CD115-APC (AFS98) (1/50, Biolegend catalog no. 135510); CD31-PE (MEC 13.3) (1/100, BD Pharmingen catalog no. 553373); Tie2 CD202b-PE (TEK4) (1/200, eBioscence catalog no. 12-5987-81); CD88-PE (20/70) (1/200, Biolegend catalog no. 135806); CD88-APC (20/70) (1/100, Biolegend catalog no. 135808); CCR2-Alexa Fluor 647 (SA203G11) (1/100, Biolegend catalog no. 150603); CCR2-PE-Cy7 (SA203G11) (1/100, Biolegend catalog no. 150612); HO-1-PE (HO-1-2) (1/200, EnzoLifeSciences catalog no. ADI-OSA-11PE-F); CX3CR1-PE (SA011F11) (1/200, Biolegend catalog no. 149005); CD195 (CCR5)-PE (HM-CCR5) (1/100, Biolegend catalog no. 107005); TNFα-Alexa Fluor 647 (MP6-XT22) (1/100, BD Pharmingen catalog no. 557730); CD206-APC (C068C2) (1/100, Biolegend catalog no. 141708); CD64-APC (X54-5/7.1) (1/100, eBioscence catalog no. 17-0641-82); CD16/32-APC (93) (1/100, eBioscence catalog no. 17-0161-82); Hematopoietic Lineage-eFluor 450 (1/400, eBioscence catalog no. 88-7772-72); CD34 FITC (RAM34) (1/100, BD Pharmingen catalog no. 560238); Gr1-FITC (RB6-8C5) (1/50, BD Pharmingen catalog no. 553127); CD44-FITC (IM7) (1/100, Biolegend catalog no. 103006); CD62L-APC (Mel-14) (1/100, BD Pharmingen catalog no. 553152); CD62L-BV570 (Mel-14) (1/100, Biolegend catalog no. 104433); SiglecF-FITC (S17007L) (1/100, Biolegend catalog no. 155504); SiglecF-Alexa Fluor 700 (E50-2440) (1/50, BD Bioscence catalog no. 562680); Ki67-APC (16A8) (1/100, Biolegend catalog no. 652405); VEGFR-PE-Cy7 (Avas12) (1/200, Biolegend catalog no. 136414); CD163-Super Bright 702 (TNKUPJ) (1/100, eBioscence catalog no. 67-1631-82); E-Cadherin-BV421 (DECMA-1) (1/100, Biolegend catalog no. 147319). We also used unconjugated goat polyclonal anti-C3aR (D-20) (1/200, Santa Cruz Biotechnology catalog no. sc-14624); rabbit anti-pSTAT1 (58D6) (1/200, Cell Signaling catalog no. 9167); rabbit anti-pSTAT3 (M9C6) (1/200, Cell Signaling catalog no. 4113); rabbit anti-pSTAT6 (D8S9Y) (1/200, Cell Signaling catalog no. 56554); Nrf2 rabbit polyclonal antibody (1/100, ThermoFisher catalog no. PA5-27882); VEGF rabbit polyclonal antibody (SP07-01) (1/100, ThermoFisher catalog no. MA5-32038); Vimentin rabbit monoclonal antibody (SP20) (1/100, ThermoFisher catalog no. MA5-14564); N-Cadherin rabbit monoclonal antibody (3B9) (1/100, ThermoFisher catalog no. 33-3990); and anti-HIF1α rabbit monoclonal antibody (16H4L13) (1/100, ThermoFisher catalog no. 700505), followed by incubation with secondary donkey anti-goat Alexa Fluor 647-conjugated antibody (1/500, ThermoFisher catalog no. A-21447), goat anti-rabbit Alexa Fluor 488-conjugated antibodies (1/500, ThermoFisher catalog no. A-11008) and goat anti-rabbit Alexa Fluor 647-conjugated antibodies (1/500, ThermoFisher catalog no. A27040). Cell viability was determined by either Aqua LIVE/Dead-405-nm staining (1/800, Biolegend catalog no. 423102) or LIVE/DEAD Fixable Violet Dead Cell Stain Kit (1/1,000, ThermoFisher catalog no. L34960); negative cells were considered viable. A Foxp3/Transcription Factor Staining Buffer Set (eBioscience) was used for intracellular staining of TNF-α, IFNγ, Foxp3 and CD206. Expression of TNF-α and IFN-γ was analyzed by flow cytometry following 4 h of treatment with brefeldin A (5 µg ml^{-1}), PMA (50 ng ml^{-1}) and ionomycin (1 µg ml^{-1}). Cells were detected using either BD FACSCanto II, BD LSRFortessa or BD FACSymphony and analyzed with BD FACSDiva and FlowJo (9.3.2 and 9.9.6, respectively) software. Results are reported as MFI normalized on isotype control or fluorescence minus one.

Purification of mouse leukocytes. Thioglycollate-elicited PECs were isolated from healthy mice as previously described[3]. PECs were cultured in RPMI 1640 medium supplemented with 10% FBS, 2 mM glutamine and 100 U ml^{-1} penicillin/streptomycin. To induce LPS tolerance, cells were incubated in the presence of LPS (100 ng ml^{-1}) (LPS from *Salmonella abortus* Equi S-form; Alexis) for 20 h, washed, maintained in RPMI medium for 2 h and then rechallenged with LPS for 4 h (LPS/LPS, L/L). To induce M1 activation, cells were incubated in medium for 20 h, washed, left in medium for 2 h and finally stimulated with LPS for 4 h (medium/LPS, M/L). Control cells (medium/medium, M/M) were cultured in medium for the duration of the experiment. Where indicated, PECs were pretreated with either ZnPPIX (2 µM, Frontier Scientific) or CORM-2 (10 µM, Frontier Scientific) for 2 h before induction of LPS tolerance. Where indicated, PECs from WT or *p50*$^{-/-}$ mice were treated with 100 ng ml^{-1} of either C3a (R&D Systems) or M-CSF (Peprotech) for 24 and/or 48 h.

Primary tumors were cut into small pieces, disaggregated with 0.5 mg ml^{-1} COL IV and 150 U ml^{-1} DNase I in RPMI 1640 for 30 min at 37 °C and filtered through strainers. TAMs isolated 3–4 weeks after tumor implantation, as previously described[45], were enriched by positive selection using CD11b microbeads (MACS, Miltenyi Biotec) according to the manufacturer's instructions. The purity of CD11b$^+$ cells was ~90% as determined by FACS. To obtain high-purity TAM populations (that is, F4/80^{hi}C5aR1^{hi} and F4/80^{lo}C5aR1^{lo}, respectively), CD11b$^+$ cells were stained (CD45-PerCP, F4/80-APC, CD88-PE) and sorted on a FACSAria cell sorter (BD Bioscience). The purity of each population was ≥90%. The resulting cells were either processed for mRNA extraction or used for adoptive transfer or migration experiments in vitro.

Quantitative PCR. Total RNA was extracted using Trizol reagent (Invitrogen) following the manufacturer's instructions. Complementary DNA was synthesized by reverse transcription using a High Capacity cDNA Archive Kit (Applied Biosystems), and quantitative real-time PCR was performed using SybrGreen PCR Master Mix (Applied Biosystems) in a 7900HT Fast Real-Time System (Applied Biosystems). Data were processed using SDS v.2.2.2 software (Applied Biosystems) and analyzed with the $2^{(-\Delta CT)}$ method. Data were normalized to *β-actin* or *GAPDH* expression. Primer sequences used in the manuscript are available upon request.

Confocal microscopy. Frozen tissues in OCT (optimal cutting temperature compound) were sectioned (8 µm), mounted on positively charged slides, air-dried for 30 min and fixed with 4% paraformaldehyde for 10 min at room temperature. Sections were permeabilized with 0.1% Triton X-100 and incubated with blocking buffer (5% normal goat serum, Sigma-Aldrich, 2% BSA, 0.05% Tween). Slides were then stained with rabbit anti-mouse/human HO-1 (1 µg ml^{-1}; Bio-Rad catalog no. 4915-1050) and rat anti-mouse F4/80 (1 µg ml^{-1}; Bio-Rad catalog no. MCA497R) or rabbit anti-mouse CD31 (0.5 µg ml^{-1}; PECAM-1, Pharmingen) followed by Alexa Fluor 488-conjugated goat anti-rabbit IgG (1/1,000, ThermoFisher, catalog no. A-11008) and Alexa Fluor 647-conjugated goat anti-rat IgG antibody (1/1,000, ThermoFisher catalog no. A21-247). Nuclei were counterstained with DAPI (Invitrogen catalog no. D1306). Coverslips were mounted with the antifade medium FluorPreserve Reagent (EMD Millipore) and analyzed with an Olympus Fluoview FV1000 (FV10-ASW 3.0) laser scanning confocal microscope using the fine-focus oil immersion lens (×4/1.3 numerical aperture (NA)) at resolution of 1 Airy unit and operating in channel mode with excitation 405 and 633 nm (×4/1.3 NA Plan-Apochromat; Olympus).

Immunoblotting. After the indicated treatments, PECs or TAMs were lysed in 50 µl of lysis buffer (20 mM Tris-HCl pH 8.0, 137 mM NaCl, 10% glycerol (vol/vol), 1% Triton X-100 (vol/vol), 1 mM Na$_3$VO$_4$, 2 mM EDTA, 1 mM phenylmethyl sulfonyl fluoride, 20 µM leupeptin and 0.15 U ml^{-1} aprotinin) for 20 min at 4 °C. The lysates were centrifuged at 13,000g at 4 °C for 15 min, and the supernatants were run on 10% (wt/vol) SDS–polyacrylamide gel electrophoresis (SDS–PAGE; 30 µg of protein per lane). Separated proteins were transferred to a nitrocellulose membrane and immunoblotted for specific antibodies according to the manufacturer's instructions. The following antibodies were used: (primary) rabbit anti-mouse phospho-p44/42 MAPK (Erk1/2; Cell Signaling Technologies) and goat anti-mouse vinculin (Santa Cruz Biotechnology); (secondary) goat anti-mouse and anti-rabbit IgG horseradish peroxidase (HRP)-conjugated (Amersham). ImageLab Software v.4.1 (Bio-Rad) was used for image acquisition and densitometric analysis of blots.

In vitro migration assay. Migration of PECs and TAMs was evaluated using a previously described chemotaxis microchamber technique[4]. Briefly, 30 µl of 100 ng ml^{-1} chemoattractant solution (C5a or C3a, both R&D Systems) in RPMI 1640 with 1% FBS, or control medium (RPMI 1640 with 1% FBS), was added to the lower wells of a chemotaxis Boyden chamber (Neuroprobe) and a polycarbonate filter (polyvinyl polypyrrolidone-treated, 5 µm pore size; Neuroprobe) was placed in the wells and covered with a silicon gasket. The correct concentration for each cytokine used was determined by dose–response assay using WT or $p50^{-/-}$ cells (Extended Data Fig. 1c). Fifty microliters of cell suspension (4×10^6 ml^{-1}) was seeded in the upper wells and the chamber was incubated at 37 °C for 4 h. Filters were then removed and stained with Diff-Quik (Baxter). Ten high-power oil immersion fields were counted.

Immunohistochemistry and image analysis. Immunohistochemistry on formalin-fixed, paraffin-embedded (PFPE) tissues from human melanoma lesions was performed as described previously[46]. Sections were stained with antibodies to CD3 (no. NCL-L-CD3-PS1, Leica Biosystems), CD68 (no. M0814, Dako), CD163 (no. NB110-59935, Novus Biologicals) and HO-1 (no. ab13248, Abcam). Images were acquired at ×20 with an Aperio Scanscope XT digital pathology slide scanner (Leica Biosystems). Quantitative assessment of HO-1$^+$ cells was performed using open source QuPath software v.0.1.2. Files in .svs format, generated by Aperio Scanscope, were preprocessed by the 'auto detect' function of the visual stain editor to estimate staining vectors after selection of an area containing background and strong hematoxylin and DAB staining. Regions of interest (ROI), each containing at least 10,000 cells and collectively representing an average surface area of 2–3 mm^2 of each lesion, were defined for subsequent positive cell detection. The score compartment was 'cytoplasm DAB OD mean' for HO-1 staining. A single threshold for intensity (0.2) was adopted. QuPath annotation measurements, including number of negative or positive cells and area (in µm^2) of each ROI, were exported to Excel for further analysis. For anti-mouse CD31, F4/80 and HO-1, PFPE mouse tumor tissues were mounted on Super-frost slides, dewaxed in xylene and rehydrated in ethanol. Endogenous peroxidases were blocked for 20 min with 2% H_2O_2. Unspecific binding sites were blocked with PBS + 2% BSA for 1 h. Tissues were incubated for 2 h with affinity-purified immunoglobulin against CD31 (0.5 µg ml^{-1} PECAM-1, Pharmingen), anti-mouse F4/80 (Clone CI:A3-1, 1/500, Bio-Rad catalog no. MCA497R) or anti-mouse HO-1 (1/500, Bio-Rad catalog no. 4915-1050) in PBS supplemented with BSA (2%). Either a Rat-on-Mouse HRP polymer kit (no. RT517H, Biocare Medical) or MACH1 Universal HRP polymer detection kit (no. M1U539 G, Biocare Medical) was used as secondary antibody. Reactions were developed with 3,3-diaminobenzidine (Biocare Medical) and slides were then counterstained with hematoxylin and mounted with Eukitt mounting medium (Sigma-Aldrich).

In vivo vascular permeability assay and confocal microscopy. FITC–labeled 40-*kDa* dextran (0.25 mg per mouse; ThermoFisher Scientific/Life Technologies) was administered intravenously by retro-orbital injection into anesthetized MN/MCA1-bearing mice. Thirty minutes after injection, mice were perfused with PBS and tumors were fixed in 2% paraformaldehyde and embedded in OCT. Specimens were permeabilized with 0.1% Triton X-100 and incubated with blocking buffer (5% normal goat serum (Sigma-Aldrich), 2% BSA, 0.05% Tween). The following primary antibodies were used: rat anti-mouse CD31 (no. MEC 13.3, 0.5 µg ml^{-1}; BD Biosciences), Cy3TM-labeled anti-α-SMA (no. 1A4, 2 µg ml^{-1}; Sigma-Aldrich) and rabbit anti-COL IV (no. PA1-28534, 1 µg ml^{-1}; ThermoFisher Scientific). A goat anti-rat antibody conjugated with Alexa Fluor 647 (ThermoFisher Scientific, catalog no. A21-247) and a goat anti-rabbit antibody conjugated with Alexa Fluor 532 (ThermoFisher Scientific, catalog no. A11-009) were respectively used to detect CD31 and COL IV. Coverslips were mounted with the antifade medium FluorPreserve Reagent (EMD Millipore) and analyzed with a Leica SP8 STED3X confocal microscope system and a multi-immersion HP PL ×20/NA 0.75 lens equipped with a white light laser (Leica Microsystems). Images (*xyz*, 1,024 × 1,024 pixels) were acquired in unidirectional mode as a mosaic (15–30 images per condition) to cover entire tumor specimens and were analyzed as a maximum-intensity projection. A similar background correction was applied to all samples for each staining. Vessel leakiness under different conditions was assessed as colocalization rate between the extracted signal of CD31$^+$ and FITC$^+$ pixels by LASX software (v.3.5.7, Leica Microsystems), using the same threshold and expressed percentage of colocalization material. Similarly, pixels referring to markers of vessel stability, α-SMA and COL IV, were separately analyzed as colocalization rate with CD31$^+$ vessels.

Microarray analysis. Total RNA was extracted from $1–5\times10^6$ PECs and F4/80^{hi} and F4/80^{lo} TAMs (RNeasy kit, Qiagen) according to standard methods. Samples were amplified, labeled using the Agilent Quick Amp labeling kit and hybridized using Agilent SurePrint G3 Mouse GE 8x60K Microarray (no. G4852A-028005, Agilent Technologies) and Agilent SureHyb hybridization chambers. Three independent replicate experiments were performed for each group. Scanned images were analyzed with Feature Extraction Software (v.10.7, Agilent Technologies) using default parameters to obtain filtered, background-subtracted and quantile-normalized spatially processed signal intensities. log$_2$ normalized intensity signals were imported into R software (v.3.5.1) with Bioconductor (v.3.8) and further processed with the limma package (v.3.38)[47]. The BiomaRt package (v.2.40)[48] was used to annotate probe ID with the Agilent SurePrint G3 GE 8 × 60-k probe annotation set. Resulting log$_2$ normalized intensity values for the 9.703 unique probes and corresponding genes are provided in Supplementary Table 1. Differential expression analysis: the limma package was used to calculate fold changes and *P* values for differential expression using the empirical Bayes statistics for differential expression (eBayes) framework. A probe was considered significantly differentially expressed if it had an absolute value of fold change ≥1.5 and adjusted $P \leq 0.05$. A complete list of all 5,587 differentially expressed genes is provided in Supplementary Table 1. Hierarchical clustering and heatmaps were performed using the pheatmap R package (v.1.0.12); Principal component analysis was performed using the R packages factoextra (v.1.0.6) and FactoMineR (v.1.42). Gene expression levels were centered on the mean and normalized. Clustering was done using complete linkage with Euclidean distance as the metric. GO analysis was done with enrichGO from the R package ClusterProfiler (v.3.10.1)[49] providing the GO gene set (c5.bp.v.6.2) retrieved from the Molecular Signatures Database[50]. A term was considered significantly enriched with adjusted $P \leq 0.1$.

Statistics and survival analysis. Data relative to patients and biomarker (HO-1 gMFI values in 15 monocyte subsets) characteristics are presented by group (discovery, confirmation) and overall. Summary measures were relative and absolute frequencies for categorical data, and mean median range and interquartile range for continuous data. Comparison of biomarker distribution between groups was conducted by means of the Wilcoxon test for independent groups. Association of biomarkers with survival was tested by a semiparametric Cox regression model in both the univariate and multivariable approach, adjusted for postoperative therapy (at the time of blood sample isolation). Hazard ratio relative to a variation per unit of the scale was calculated, together with 95% confidence interval and associated *P* value. Analysis was conducted in the discovery group and then validated in the confirmation group. Kaplan–Meier survival curves were calculated for each biomarker (HO-1 gMFI value in each of the 15 monocyte subsets), considering the overall median of the distribution of values of each biomarker as the cutoff point for dichotomization. Deviation from Gaussian distribution of HO-1 gMFI values of all monocyte subsets was assessed using the D'Agostino–Pearson omnibus normality test. Comparison of discovery and confirmation sets for HO-1 gMFI values in monocytes was carried out by Mann–Whitney test. Comparison of multiple samples was carried out by Kruskal–Wallis test followed by Dunn's multiple comparison tests. Survival was defined as the time (days) from peripheral blood isolation (coincident with surgery for metastatic disease) to death or the date of last information on patient status. For animal studies, sample size was defined based on experience on cancer and infection models, which enabled us to detect differences of 20% or greater between groups (10% I-type error and 80% power). Values are expressed as either mean ± s.e.m. or median of biological replicates. Either one-way ANOVA or a Kruskal–Wallis test was used to compare multiple groups. A two-tailed, unpaired Student's *t*-test was used to compare unmatched groups with Gaussian distribution. A Mann–Whitney *U*-test was used in cases of non-Gaussian distribution. Two-way ANOVA corrected for multiple comparison by Šidák's test was used to take into account multiple comparisons. $P \leq 0.05$ was considered statistically significant. Statistical analyses were performed with GraphPad Prism v.7 GraphPad Software and SAS software, v.9.4 (SAS Institute).

Timer analysis. Results of the multivariable Cox proportional hazards model on the TCGA skin cutaneous melanoma dataset were obtained through the outcome module of the TIMER2.0 web server (available at http://timer.comp-genomics.org)[51] by testing the relevance of tumor-infiltrating macrophages, as identified by the M2_TIDE macrophage signature[52], and of the expression of macrophage-related genes CD163, HMOX1 and CD68.

Reporting Summary. Further information on research design is available in the Nature Research Reporting Summary linked to this article.

Data availability

The data that support the findings of this study are available from the corresponding author upon reasonable request. RNA-seq raw data are reported in Supplementary Table 1 and have been deposited at the Gene Expression Omnibus (GEO accession no. GSE167413). Datasets containing patients' clinical parameters and flow cytometry data generated during the current study are presented in Supplementary Tables 2 and 3.

References

42. Nemeth, Z. et al. Heme oxygenase-1 in macrophages controls prostate cancer progression. *Oncotarget* **6**, 33675–33688 (2015).
43. Chan, K., Lu, R., Chang, J. C. & Kan, Y. W. NRF2, a member of the NFE2 family of transcription factors, is not essential for murine erythropoiesis, growth, and development. *Proc. Natl Acad. Sci. USA* **93**, 13943–13948 (1996).

44. Carminati, L. et al. Antimetastatic and antiangiogenic activity of trabectedin in cutaneous melanoma. *Carcinogenesis* **40**, 303–312 (2019).
45. Biswas, S. K. et al. A distinct and unique transcriptional program expressed by tumor-associated macrophages (defective NF-κB and enhanced IRF-3/STAT1 activation). *Blood* **107**, 2112–2122 (2006).
46. Sensi, M. et al. Immunogenicity without immunoselection: a mutant but functional antioxidant enzyme retained in a human metastatic melanoma and targeted by CD8$^+$ T cells with a memory phenotype. *Cancer Res.* **65**, 632–640 (2005).
47. Ritchie, M. E. et al. limma powers differential expression analyses for RNA-sequencing and microarray studies. *Nucleic Acids Res.* **43**, e47 (2015).
48. Durinck, S., Spellman, P. T., Birney, E. & Huber, W. Mapping identifiers for the integration of genomic datasets with the R/Bioconductor package biomaRt. *Nat. Protoc.* **4**, 1184–1191 (2009).
49. Yu, G., Wang, L. G., Han, Y. & He, Q. Y. clusterProfiler: an R package for comparing biological themes among gene clusters. *OMICS* **16**, 284–287 (2012).
50. Subramanian, A. et al. Gene set enrichment analysis: a knowledge-based approach for interpreting genome-wide expression profiles. *Proc. Natl Acad. Sci. USA* **102**, 15545–15550 (2005).
51. Li, T. et al. TIMER: a web server for comprehensive analysis of tumor-infiltrating immune cells. *Cancer Res.* **77**, e108–e110 (2017).
52. Jiang, P. et al. Signatures of T cell dysfunction and exclusion predict cancer immunotherapy response. *Nat. Med.* **24**, 1550–1558 (2018).

Acknowledgements

This work was supported by Associazione Italiana per la Ricerca sul Cancro (AIRC) IG (nos. 19885 to A.S. and 15860 to R.M.); AIRC 5x1000 no. 22757; Fondazione Cariplo and Ministero Universita Ricerca (project no. 2017BA9LM5_001); AIRC fellowship 'Pierluigi Meneghelli' (no. 19682); Associazione "Augusto per la Vita" Novellara (RE); and Associazione "Medicine Rocks", Milano. We thank C. Vegetti and I. Bersani (Fondazione IRCCS Istituto Nazionale dei Tumori) for excellent technical help with flow cytometry analysis of human monocyte subsets and immunohistochemistry of melanoma lesions, respectively. We also thank M. Soares for critical discussions and editing of the manuscript. M.P.S. is supported by Fundação 'la Caixa', Fundação para a Ciência e Tecnologia (nos. HR18-00502 and SAICT/2017/029411).

Author contributions

F.M.C., M.G.T., A.B. and F.P. played a key role in designing and conducting most of the experiments. M. Storto provided technological support with in vivo experiments. M.F. and L.G. performed genomic analysis of myeloid populations. P.K. and A.T. provided bioinformatics analysis of genomics data. C.A. and C.P. contributed to experiments. M.E. and A.D. performed immunofluorescence analysis on murine samples. R.M., A.A., F.S., G.G. and M.M. performed flow cytometric analysis and/or immunohistochemical analysis of specimens from patients with melanoma. M. Santinami and A.M. assessed clinical condition and provided biological tissues from patients with melanoma. E.R. and V.T. performed statistical and survival analysis in the discovery and confirmation sets stratified by monocyte subset-specific HO-1. M.P.S. contributed by provision of reagents and critical discussions on the experimental results. A.A., F.M.C. and A.S. drafted the manuscript. A.S. provided the guiding hypothesis of the work and contributed to the experimental design and supervision of the study.

Competing interests

The authors declare no competing interests.

Additional information

Extended data is available for this paper at https://doi.org/10.1038/s41590-021-00921-5.

Supplementary information The online version contains supplementary material available at https://doi.org/10.1038/s41590-021-00921-5.

Correspondence and requests for materials should be addressed to A.S.

Peer review information *Nature Immunology* thanks Daniele Gilkes, Hozumi Motohashi and the other, anonymous, reviewer(s) for their contribution to the peer review of this work. Zoltan Fehervari was the primary editor on this article and managed its editorial process and peer review in collaboration with the rest of the editorial team.

Reprints and permissions information is available at www.nature.com/reprints.

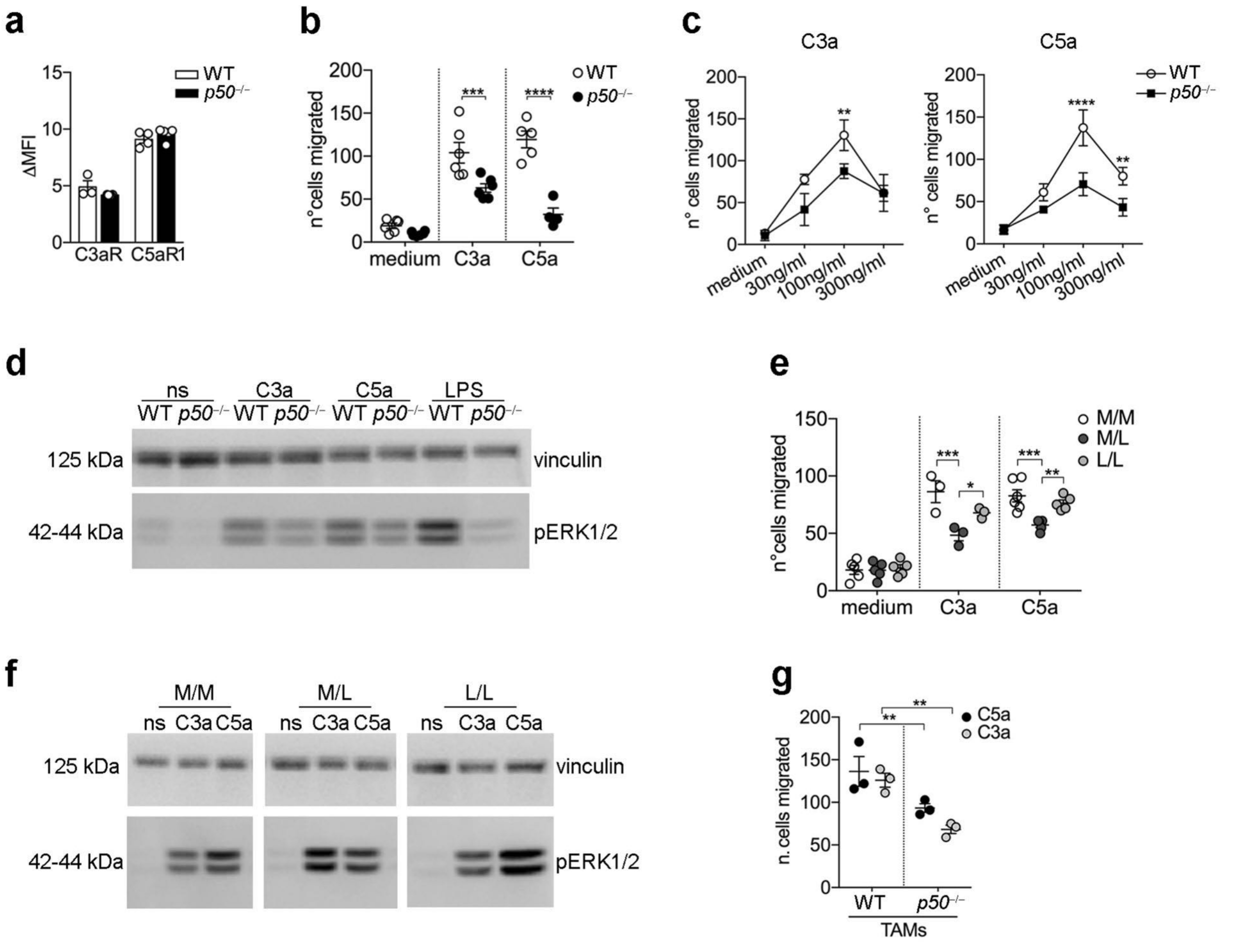

Extended Data Fig. 1 | Role of NF-κB1 in macrophage migration. a, FACS analysis of C5aR1, and C3aR in WT and *p50*$^{-/-}$ PECs (Δ=variation compared to isotype control), $n=4$ mice per genotype; shown are data representative of two independent experiments. **b**, Boyden-chamber migration assay of WT and *p50*$^{-/-}$ PECs in response to C3a or C5a; shown are pooled data from $n=2$ experiments with $n=3$ animals per group. **c**, Bell-shaped curve migration of WT and *p50*$^{-/-}$ PECs in response to C3a and C5a, for each condition, cells pooled from $n=3$ mice were used; one experiment was performed. **d**, Phospho-ERK1/2 levels in WT and *p50*$^{-/-}$ PECs treated with C3a, C5a or LPS, for each condition, cells pooled from $n=3$ mice were used; one experiment was performed. **e**, Chemotactic activity of WT PECs: untreated (M/M); LPS-activated: 20 h medium plus 4 h LPS (M/L); LPS-tolerant: 20 h LPS plus 4 h restimulation with LPS (L/L); medium and C5a: shown are pooled data from $n=2$ experiments with $n=3$ animals per group, C3a: $n=3$ mice were used, one experiment was performed. **f**, immunoblot analysis of phospho-ERK1/2 in M/M, M/L and L/L PECs in response to C3a or C5a treatment, for each condition, cells pooled from $n=3$ mice were used; one experiment was performed. **g**, Boyden-chamber migration assay of TAMs (CD45$^+$F4/80$^+$CD11b$^+$) FACS-sorted from WT or *p50*$^{-/-}$ MN/MCA1 tumor-bearing mice. For each condition, cells pooled from $n=3$ mice were used; one experiment was performed. Data are mean ± SEM. *$P<0.05$ **$P<0.01$ ***$P<0.001$, ****$P<0.0001$ between selected relevant comparisons. In **a-g**, two-way ANOVA with Sidak's multiple comparisons test.Source data

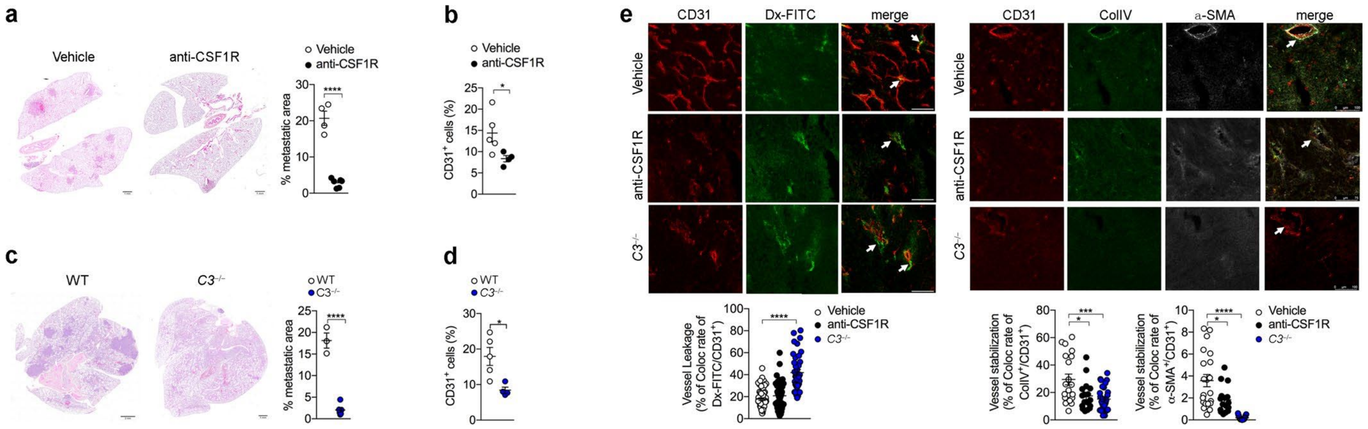

Extended Data Fig. 2 | Impact of F4/80^{hi} TAMs accumulation on metastasis formation and tumor angiogenesis. **a**, area of metastatic burden quantified from H&E stained lung sections from WT MN-MCA1-bearing mice treated with vehicle or anti-CSF1R is expressed as a percentage of total lung surface area. Representative images are shown. Scale bars, 1 mm. $n=4$ (Vehicle) and $n=5$ (anti-CSF1R), one experiment was performed. **b**, FACS quantification of CD31$^+$ cells in lung metastasis of WT MN-MCA1-bearing mice treated with vehicle or anti-CSF1R; $n=5$ (Vehicle) and $n=4$ (anti-CSF1R), shown are data representative of two independent experiments. **c**, Representative H&E stained lung sections from WT and *C3*$^{-/-}$ MN-MCA1-bearing mice and quantification of area of metastatic burden expressed as a percentage of total lung surface area. Scale bars, 1 mm. $n=3$ (Vehicle) and $n=5$ (*C3*$^{-/-}$), one experiment was performed. **d**, FACS quantification of CD31$^+$ cells in lung metastasis of WT and *C3*$^{-/-}$ MN-MCA1-bearing mice; $n=5$ (Vehicle) and $n=4$ (*C3*$^{-/-}$), shown are data representative of two independent experiments. **e**, Representative images of MN/MCA1 tumor sections from WT, *C3*$^{-/-}$ and anti-CSF1R treated mice injected with FITC-Dextran. Sections were co-stained for FITC-Dextran (green) and CD31 (red) (top left); quantification of vascular permeability expressed as percentage of colocalization rate between extracted signal of CD31$^+$ and FITC$^+$ pixels (bottom left). Representative images of MN/MCA1 tumor sections from WT, *C3*$^{-/-}$ and anti-CSF1R treated mice costained for collagen IV (green), CD31 (red) and α-SMA (white) (top right); quantification of vessel stability was assessed as colocalization rate of Collagen IV$^+$ or α-SMA$^+$ with CD31$^+$ vessels (bottom right); scale bars, 10 μm; $n=3$ mice per genotype, one experiment was performed. Data are mean ± SEM. $^*P<0.05$ $^{**}P<0.01$ $^{***}P<0.001$, $^{****}P<0.0001$ between selected relevant comparisons. In **a-d**, two-tailed unpaired Student's t-test. In **e**, one-way ANOVA and Kruskal-Wallis test with Dunn's multiple comparisons test.

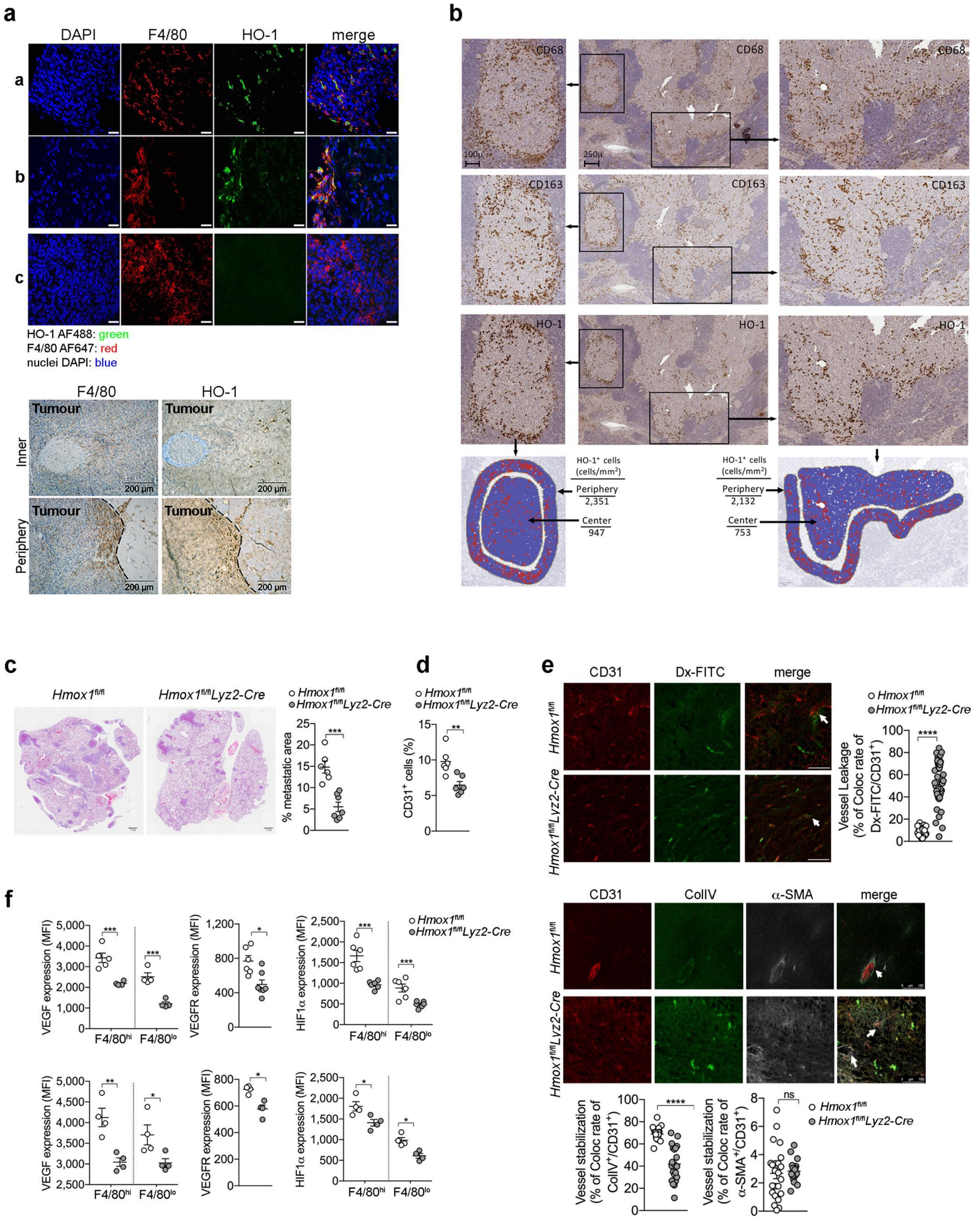

Extended Data Fig. 3 | See next page for caption.

Extended Data Fig. 3 | Impact of F4/80^{hi} HO-1^{+} TAMs accumulation at the invasive tumor margin on metastasis formation and tumor angiogenesis. **a**, (top) Representative confocal microscopy of WT MN/MCA1 tumor sections (a-b: peripheral marginal zone; c: inner area). F4/80 (red), HO-1 (green), nuclei (DAPI, blue). Representative images are shown, scale bars are 10 µm, *n* = 5 mice, one experiment was performed. (bottom) Expression of HO-1 in WT MN/MCA1 tumor sections (top: inner area; bottom: periphery). Consecutive sections from the same formalin-fixed paraffin-embedded (FFPE) lesion were stained for F4/80 and HO-1. Scale bars are 200 µm, *n* = 4 mice, one experiment was performed. **b**, Expression of HO-1 in the neoplastic tissue of a lymph node metastasis from a melanoma patient. The analysis is representative of *n* = 5 patients, one experiment was performed. Left panels, Consecutive sections from the same FFPE lesion were stained for CD68, CD163 and HO-1. Middle panels, Low magnification images showing cell staining for the three markers. Right panels, Higher magnification images of the indicated areas. Two bottom panels, quantitative analysis of the spatial distribution of HO-1^{+} cells by QuPath software (HO-1^{+} cells: red, HO-1^{-} cells: blue). **c**, area of metastatic burden quantified from H&E stained lung sections from *Hmox1*$^{fl/fl}$ and *Hmox1*$^{fl/fl}$*Lyz2-Cre*- bearing mice expressed as a percentage of total lung surface area. Representative images are shown. Scale bars, 1 mm. *n* = 6 (*Hmox1*$^{fl/fl}$) and *n* = 7 (*Hmox1*$^{fl/fl}$*Lyz2-Cre*), one experiment was performed. **d**, FACS quantification of CD31^{+} cells in lung metastasis of *n* = 6 *Hmox1*$^{fl/fl}$ and *n* = 6 *Hmox1*$^{fl/fl}$*Lyz2-Cre* MN/MCA1-bearing mice; one experiment was performed. **e (top, left)**, Representative images of MN/MCA1 tumor sections from *Hmox1*$^{fl/fl}$ and *Hmox1*$^{fl/fl}$*Lyz2-Cre* mice injected with FITC-Dextran. Sections were co-stained for FITC-Dextran (green) and CD31 (red); (top, right) quantification of vascular permeability; (bottom) Representative images of MN/MCA1 tumor sections from *Hmox1*$^{fl/fl}$ and *Hmox1*$^{fl/fl}$*Lyz2-Cre* mice co-stained for collagen IV (green), CD31 (red) and α-SMA (white) and quantification of vessel stability, *n* = 3 mice per genotype, one experiment was performed. **f**, FACS quantification of VEGF, HIFα in TAMs subsets and VEGFR in CD31^{+} cells in tumors (top) and lung metastasis (bottom) of *Hmox1*$^{fl/fl}$ and *Hmox1*$^{fl/fl}$*Lyz2-Cre* MN/MCA1-bearing mice; *n* = 5 mice per genotype (tumor), *n* = 4 mice per genotype (metastasis), one experiment was performed. Data are mean ± SEM. $^{*}P < 0.05$ $^{**}P < 0.01$ $^{***}P < 0.001$, $^{****}P < 0.0001$ between selected relevant comparisons. In **c-d-e(top)-f**, two-tailed unpaired Student's t-test. In **e (bottom)**, two-way ANOVA with Sidak's multiple comparisons test.

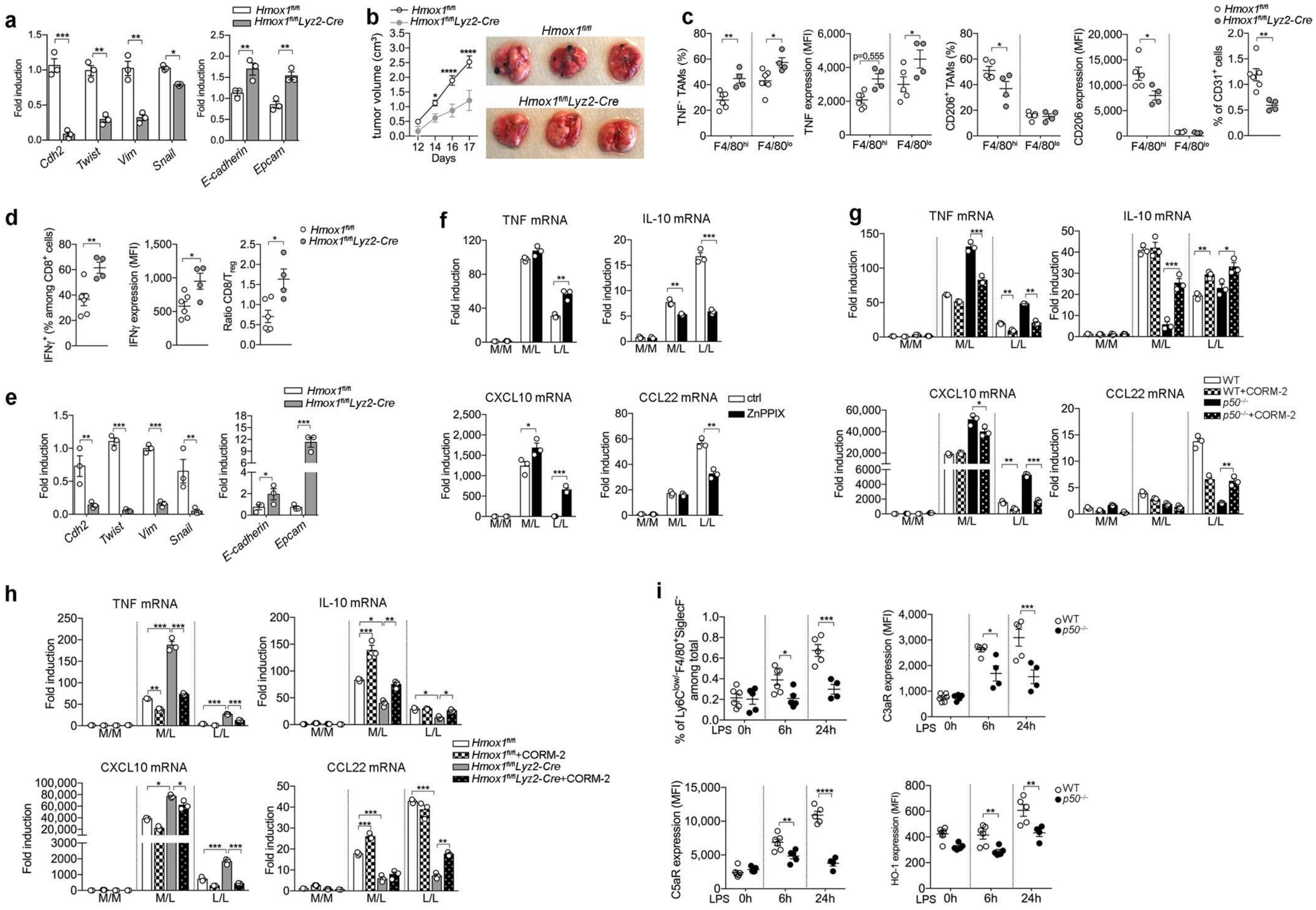

Extended Data Fig. 4 | Impact of HO-1 on tumor growth, EMT and LPS-treated macrophages. **a**, Expression of EMT-related genes in MN/MCA1 tumor cells FACS-sorted from *Hmox1*$^{fl/fl}$ and *Hmox1*$^{fl/fl}$*Lyz2-Cre* mice, shown are pooled data from $n = 3$ animals per genotype. **b**, (left) Growth of B16 melanoma in *Hmox1*$^{fl/fl}$ and *Hmox1*$^{fl/fl}$*Lyz2-Cre* mice; shown are pooled data from $n = 2$ independent experiments with $n = 5$ *Hmox1*$^{fl/fl}$ and $n = 4$ *Hmox1*$^{fl/fl}$*Lyz2-Cre* animals per group; (right) macroscopic appearances of lung metastasis are shown; $n = 3$ mice per genotype. **c**, Frequency of TNF^{+} and CD206^{+} in TAMs subsets and CD31^{+} cells; $n = 5$ (*Hmox1*$^{fl/fl}$) and $n = 4$ (*Hmox1*$^{fl/fl}$*Lyz2-Cre*) mice. **d**, Quantification of IFNγ^{+}CD8^{+} T cells and CD8 : T$_{reg}$ ratio in B16 melanoma grown in *Hmox1*$^{fl/fl}$ and *Hmox1*$^{fl/fl}$*Lyz2-Cre* mice, $n = 6$ (*Hmox1*$^{fl/fl}$) and $n = 4$ (*Hmox1*$^{fl/fl}$*Lyz2-Cre*) mice. **e**, Expression of EMT-related genes in B16 tumor cells FACS-sorted from *Hmox1*$^{fl/fl}$ and *Hmox1*$^{fl/fl}$*Lyz2-Cre* mice; shown are pooled data from $n = 3$ animals per genotype. **f**, WT PECs pre-treated or not with ZnPPIX were analyzed by RT-PCR for the expression of representative M1 and M2 cytokine genes; for each condition, cells pooled from $n = 3$ mice were used. **g-h**, PECs from WT or *p50*$^{-/-}$ mice (g) or *Hmox1*$^{fl/fl}$ and *Hmox1*$^{fl/fl}$*Lyz2-Cre* mice (h) pre-treated or not with CORM-2 were analyzed by RT-PCR for the expression of representative M1 and M2 cytokine genes. Results are given as mRNA fold increase over untreated cells (M/M); for each condition, cells pooled from $n = 3$ mice were used. **i**, Frequency of F480^{+}Ly6C$^{low/neg}$SiglecF^{-} blood monocytes and relative C5aR1, C3aR and HO-1 expression in LPS-treated WT and *p50*$^{-/-}$ mice; $n = 5$ (WT: 0h and 6h), $n = 5$ (WT: 24h, *p50*$^{-/-}$: 0h), $n = 4$ (*p50*$^{-/-}$: 6h and 24h). Data are mean ± SEM. $^{*}P < 0.05$, $^{**}P < 0.01$, $^{***}P < 0.001$, between selected relevant comparisons. In **a**, **d**, **e, f, g, h, i**, two-tailed unpaired Student's t-test. In **b, c**, two-way ANOVA with Sidak's multiple comparisons test. The data in **b (left)**, **c**, **d**, are representative of two independent experiment; in **a**, **b (right), e**, **f-i** one experiment was performed.

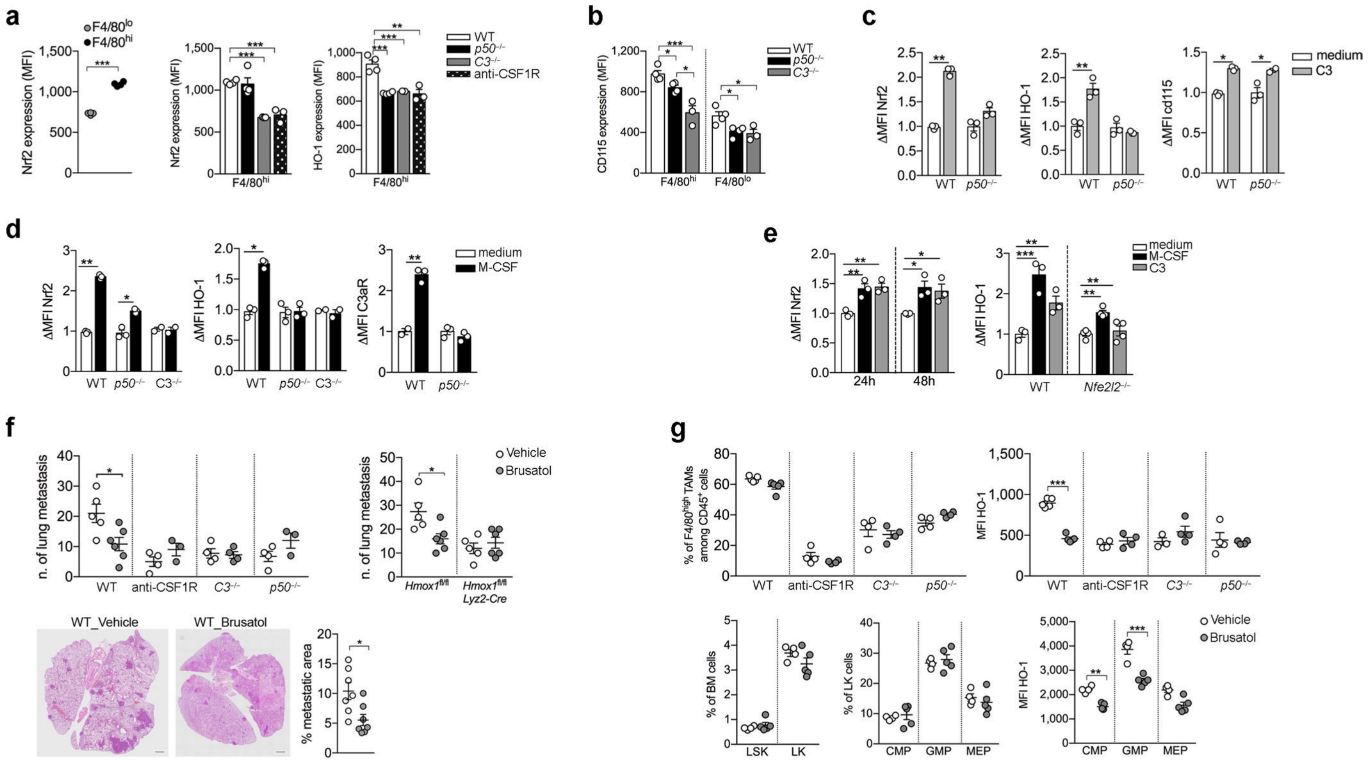

Extended Data Fig. 5 | Role of p50 NF-κB, CSF1R and C3aR in the generation of HO-1⁺ myeloid cells. **a**, FACS quantification of Nrf2 expression by F4/80^{hi} and F4/80^{lo} TAMs in WT MN/MCA1 tumors (left), *n* = 4 mice; Nrf2 and HO-1 expression by F4/80^{hi} in WT, *C3*$^{-/-}$, *p50*$^{-/-}$ and anti-CSF1R treated MN/MCA1-bearing mice (middle, right), *n* = 4 (WT, *p50*$^{-/-}$) and *n* = 3 (*C3*$^{-/-}$, anti-CSF1R) mice per group. **b**, CD115 expression of TAMs subsets in WT, *C3*$^{-/-}$ and *p50*$^{-/-}$ MN/MCA1-bearing mice, *n* = 4 (WT, *p50*$^{-/-}$) and *n* = 3 (*C3*$^{-/-}$, anti-CSF1R) mice. **c**, FACS analysis of Nrf2, HO-1 and CD115 expression in WT and *p50*$^{-/-}$ PECs stimulated or not with *C3* (Δ=variation compared to isotype control), for each condition, cells were pooled from *n* = 4 mice. **d**, FACS analysis of Nrf2, HO-1 and C3aR expression in WT, *p50*$^{-/-}$ and *C3*$^{-/-}$ PECs stimulated or not with M-CSF, for each condition, cells pooled from *n* = 4 mice were used. **e**, FACS analysis of Nrf2 and HO-1 expression in WT and *Nfe2l2*$^{-/-}$ BM-DMs stimulated or not with M-CSF and C3; for each condition, cells were pooled from *n* = 4 mice. **f**, (top) macroscopic lung metastasis quantification in WT, anti-CSF1R, *C3*$^{-/}$, *p50*$^{-/-}$ (left) and in *Hmox1*$^{fl/fl}$ and *Hmox1*$^{fl/fl}$*Lyz2-Cre* MN/MCA1 tumor-bearing mice (right), treated or not with Brusatol. (bottom) area of metastatic burden was quantified in H&E stained lung sections from WT MN-MCA1-bearing mice treated with vehicle or Brusatol and is expressed as a percentage of total lung surface area. Representative images are shown. Scale bars, 1 mm. **g**, (top) FACS quantification of F4/80^{hi} and F4/80^{lo} TAMs and relative HO-1 expression levels in WT, anti-CSF1R, *C3*$^{-/-}$, *p50*$^{-/-}$ MN/MCA1 tumor bearing mice, treated with brusatol; (bottom) percentage of LSK, LK, CMPs, MEPs and GMPs and relative HO-1 expression in the BM of untreated and brusatol-treated MN-MCA1-bearing WT mice. Data are mean ± SEM. $^{*}P < 0.05$ $^{**}P < 0.01$ $^{***}P < 0.001$, between selected relevant comparisons. In **a** one-way ANOVA or two-tailed unpaired Student's t-test. In **b–g**, two-way ANOVA with Sidak's multiple comparisons test. In **a-g**, one experiment was performed.

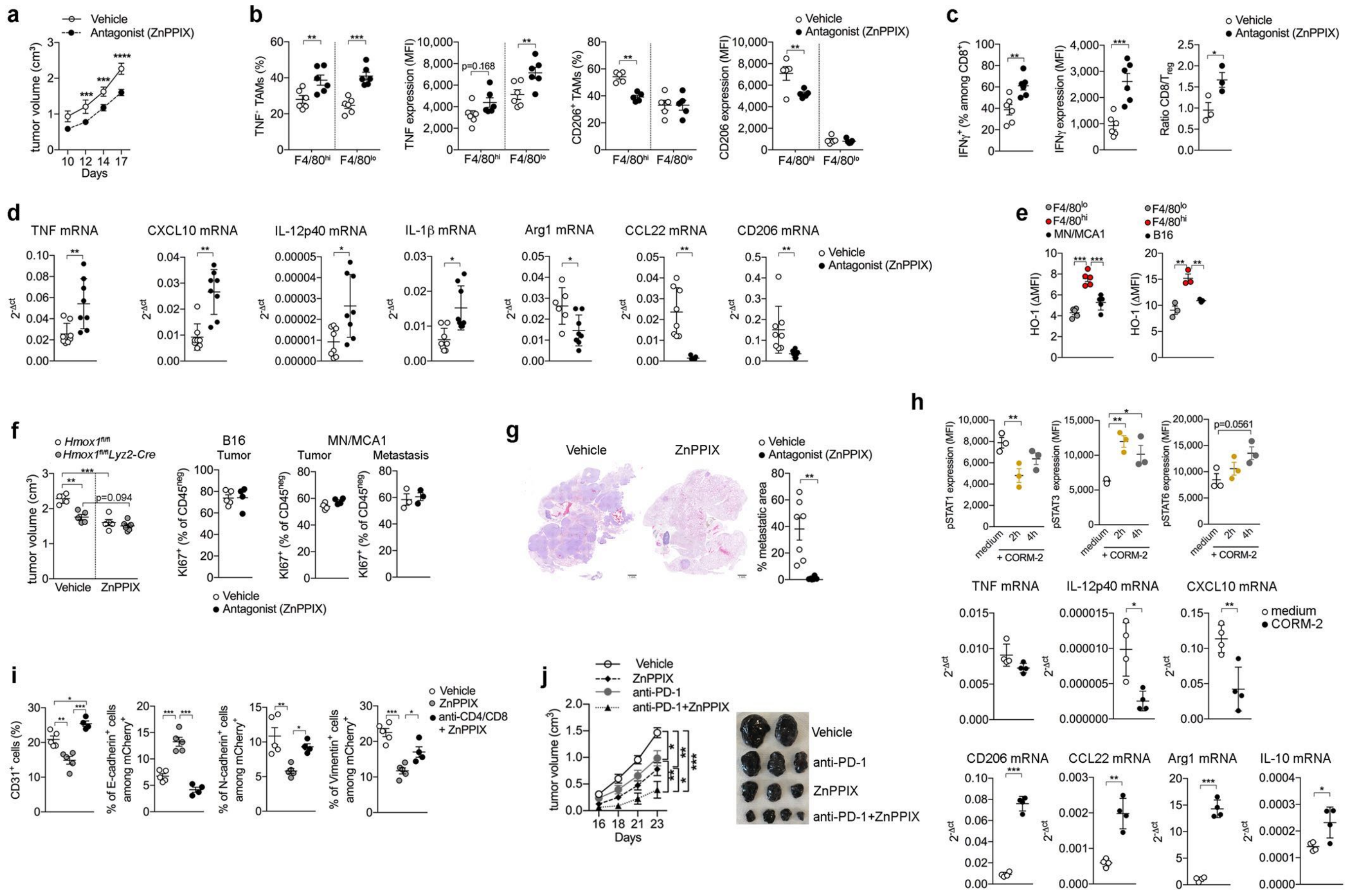

Extended Data Fig. 6 | Effects of HO-1 antagonist (ZnPPIX) on immune infiltrate and tumor growth. **a**, Mean ±- SEM tumor volume of B16 implants in WT mice treated with vehicle or ZnPPIX; *n* = 5 mice per group. **b**, FACS quantification of TNF and CD206 expression in F4/80^{hi} and F4/80^{lo} TAMs subsets; *n* = 6 mice per group. **c**, Quantification of IFNγ expression in B16 tumor-infiltrating CD8$^+$ T lymphocytes and CD8 : T$_{reg}$ ratio in vehicle- and ZnPPIX-treated mice; *n* = 5 mice per group. **d**, TAMs purified from MN/MCA1 tumors growing in WT mice treated or not with ZnPPIX were analyzed by RT-PCR for the expression of representative M1 and M2 cytokine genes; shown are pooled data from *n* = 2 technical replicates from *n* = 4 mice. **e**, FACS quantification of HO-1 expression in F4/80^{hi} and F4/80^{lo} TAMs subsets and in MN/MCA1 (left, *n* = 5 mice) or B16 tumor cells (right, *n* = 3 mice) in WT mice. **f**, (left) Mean ± SEM tumor volume of subcutaneous B16 implants in *n* = 5 *Hmox1*$^{fl/fl}$ and *n* = 5 *Hmox1*$^{fl/fl}$*Lyz2-Cre* treated with vehicle or ZnPPIX; (right) proliferation rates of B16 and MN/MCA1 cells in primary tumors and lung metastasis of mice treated with vehicle or ZnPPIX; B16: *n* = 5 (vehicle), *n* = 4 (ZnPPIX); MN/MCA1: *n* = 4 (tumor) and *n* = 3 (metastasis). **g**, Representative images of K1735-M2 lung metastasis and quantification of K1735M2 melanoma cells in C3HN mice treated or not with ZnPPIX; *n* = 7 (Vehicle) and *n* = 6 (ZnPPIX). **h** TAMs purified from MN/MCA1 tumors growing in WT mice treated or not with CORM-2 were analyzed by FACS for pSTAT1, pSTAT3, pSTAT6 expression (top, *n* = 3 mice) and by RT-PCR for the expression of representative M1 and M2 cytokine genes (bottom, *n* = 4 mice), **i**, FACS quantification of CD31$^+$ cells, E-cadherin$^+$, N-cadherin$^+$ and Vimentin$^+$ mCherry$^+$ MN/MCA1 cells in primary tumors of T lymphocyte-depleted MN-MCA1-bearing WT mice, treated or not with ZnPPIX, *n* = 5 (Vehicle and ZnPPIX) and *n* = 4 (anti-CD4/CD8+ZnPPIX). **j**, Mean ± SEM tumor volume and size of B16 tumors growing in WT mice treated with Vehicle, anti-PD-1 antibody, ZnPPIX, or anti-PD-1 antibody plus ZnPPIX are shown, *n* = 2 (Vehicle), *n* = 3 (anti-PD-1 and ZnPPIX) and *n* = 4 (anti-PD-1+ZnPPIX). Data are mean ± SEM. **P* < 0.05 ***P* < 0.01 ****P* < 0.001, between selected relevant comparisons. In **a**, **b**, **f**, **j**, two-way ANOVA with Sidak's multiple comparisons test. In **c, d**, **f**, **g**, **h**, two-tailed unpaired Student's t-test or Mann–Whitney U-test. In **e, i** one-way ANOVA and Kruskal-Wallis test with Dunn's multiple comparisons test. The data in **a–c**, are representative of two independent experiment; in **d**–**j** one experiment was performed.

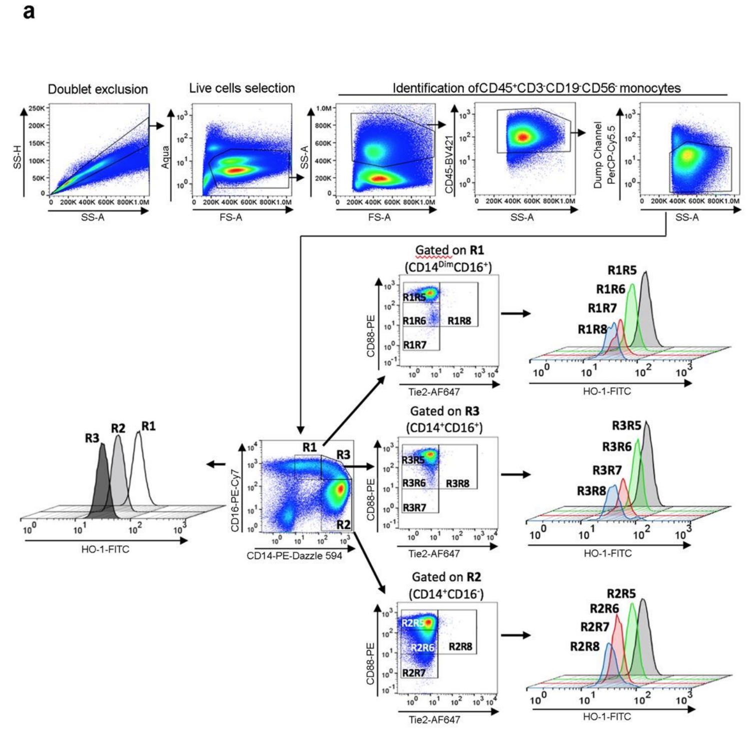

b

Monocyte subset	Phenotype	HO-1 gMFI median values Discovery cohort	Confirmation cohort	Discovery + Confirmation cohort
R1	CD14^{Dim} CD16^{+}	25.60	24.50	25.10
R2	CD14^{+} CD16^{-}	25.20	23.60	24.40
R3	CD14^{+} CD16^{+}	28.70	26.30	27.70
R1R5	CD14^{Dim} CD16^{+} CD88^{Hi} Tie2^{-}	25.30	24.40	24.80
R1R6	CD14^{Dim} CD16^{+} CD88^{+} Tie2^{-}	25.60	24.90	25.55
R1R7	CD14^{Dim} CD16^{+} CD88^{Lo} Tie2^{-}	26.80	26.65	26.70
R1R8	CD14^{Dim} CD16^{+} CD88^{+} Tie2^{+}	33.30	31.10	31.90
R2R5	CD14^{+} CD16^{-} CD88^{Hi} Tie2^{-}	24.60	23.20	23.65
R2R6	CD14^{+} CD16^{-} CD88^{+} Tie2^{-}	25.80	24.00	25.00
R2R7	CD14^{+} CD16^{-} CD88^{Lo} Tie2^{-}	25.40	23.50	24.90
R2R8	CD14^{+} CD16^{-} CD88^{+} Tie2^{+}	28.60	27.10	27.80
R3R5	CD14^{+} CD16^{+} CD88^{Hi} Tie2^{-}	28.40	25.90	27.50
R3R6	CD14^{+} CD16^{+} CD88^{+} Tie2^{-}	29.70	27.40	28.50
R3R7	CD14^{+} CD16^{+} CD88^{Lo} Tie2^{-}	30.20	28.60	29.40
R3R8	CD14^{+} CD16^{+} CD88^{+} Tie2^{+}	31.10	30.40	30.85

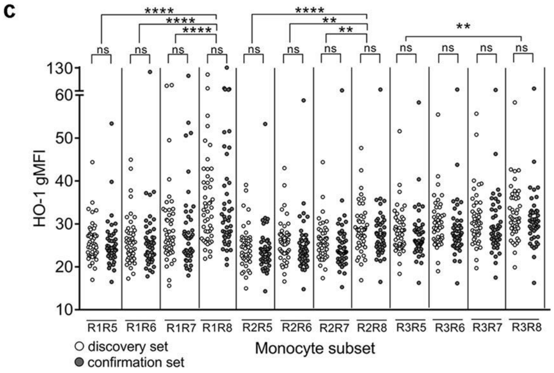

Extended Data Fig. 7 | Gating strategy for the assessment of HO-1 in peripheral blood monocyte subsets. **a**, Monocytes from peripheral blood samples were identified as CD45^{+} CD3^{-} CD19^{-} CD56^{-} cells after doublet exclusion, live cell selection and FS-A *vs.* SS-A gating (upper set of dot plots). Intracellular HO-1 expression (geometric mean fluorescence intensity, gMFI) detected in permeabilized cells was then recorded in 15 monocyte subsets (R1 to R3 and R1R5 to R3R8) defined by differential expression of CD14, CD16, CD88 and Tie-2. **b**, Median HO-1 gMFI values for each of the 15 monocyte subsets observed in peripheral blood samples from the discovery, confirmation and combined sets (discovery + confirmation). **c**, Expression of HO-1 (gMFI) in main monocyte subsets in peripheral blood samples from the discovery ($n = 47$) and confirmation ($n = 45$) sets of AJCC stage IIIC and IV melanoma patients. Statistical analysis of the combined set (discovery+confirmation cohorts) gMFI HO-1 values by Kruskal Wallis test followed by Dunn's multiple comparisons test. ns= not significant; *: $P < 0.05$; **: $P < 0.01$; ****: $P < 0.0001$.

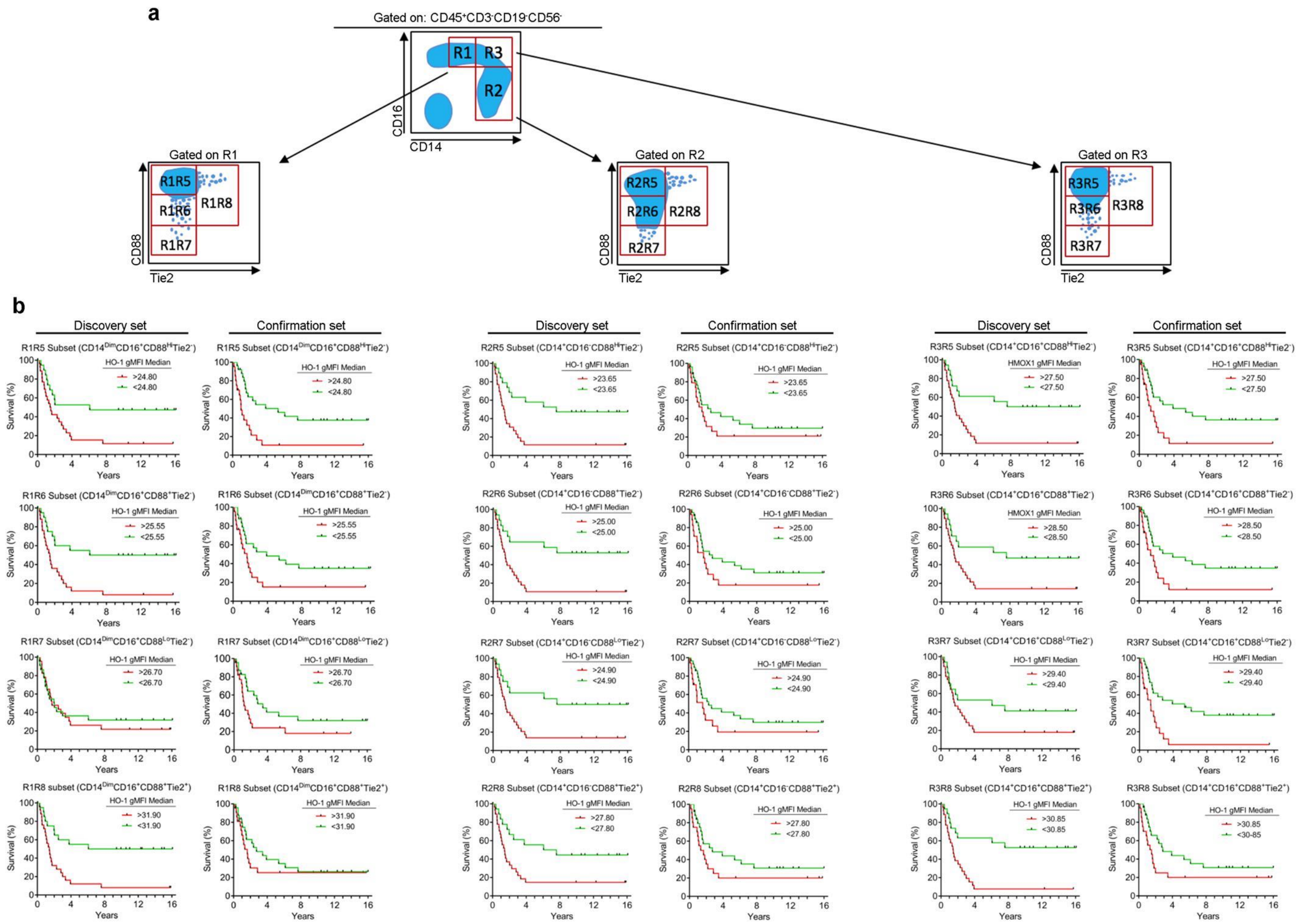

Extended Data Fig. 8 | Stratification of melanoma patients' survival based on the subset-specific median HO-1. a, Schematic of the gating strategy to identify twelve monocyte subsets (R1R5 to R3R8) in the peripheral blood of melanoma patients, based on differential expression of CD14, CD16, CD88 and Tie-2. **b**, Kaplan Meyer survival analysis in discovery and confirmation sets stratified by HO-1 gMFI higher or lower than the combined set median value observed in each monocyte subset.

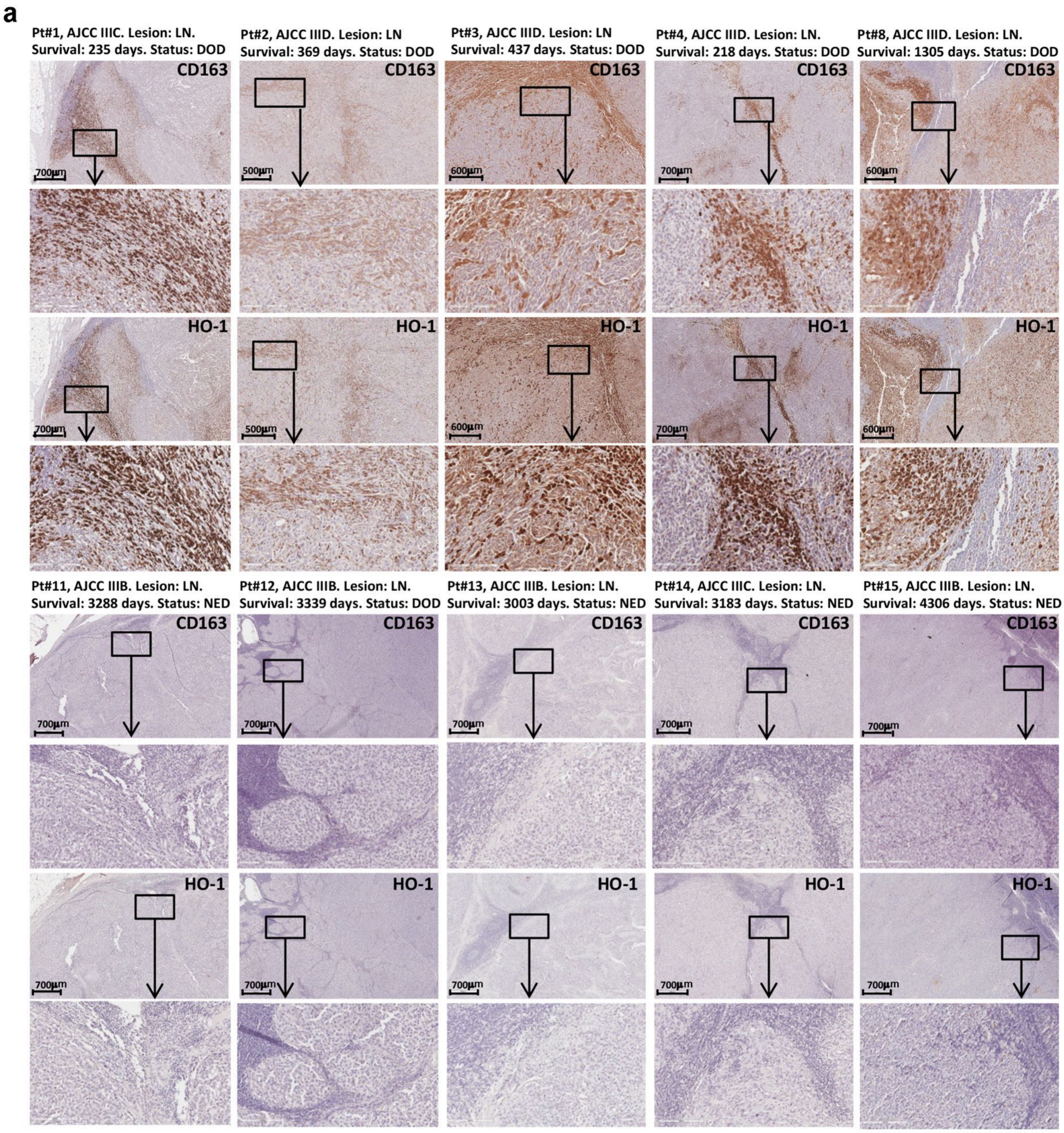

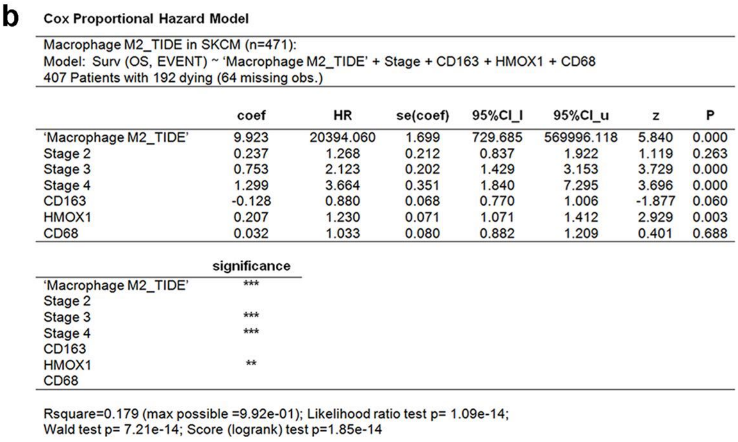

Cox Proportional Hazard Model

Macrophage M2_TIDE in SKCM (n=471):
Model: Surv (OS, EVENT) ~ 'Macrophage M2_TIDE' + Stage + CD163 + HMOX1 + CD68
407 Patients with 192 dying (64 missing obs.)

	coef	HR	se(coef)	95%CI_l	95%CI_u	z	P
'Macrophage M2_TIDE'	9.923	20394.060	1.699	729.685	569996.118	5.840	0.000
Stage 2	0.237	1.268	0.212	0.837	1.922	1.119	0.263
Stage 3	0.753	2.123	0.202	1.429	3.153	3.729	0.000
Stage 4	1.299	3.664	0.351	1.840	7.295	3.696	0.000
CD163	-0.128	0.880	0.068	0.770	1.006	-1.877	0.060
HMOX1	0.207	1.230	0.071	1.071	1.412	2.929	0.003
CD68	0.032	1.033	0.080	0.882	1.209	0.401	0.688

	significance
'Macrophage M2_TIDE'	***
Stage 2	
Stage 3	***
Stage 4	***
CD163	
HMOX1	**
CD68	

Rsquare=0.179 (max possible =9.92e-01); Likelihood ratio test p= 1.09e-14;
Wald test p= 7.21e-14; Score (logrank) test p=1.85e-14

Extended Data Fig. 9 | See next page for caption.

Extended Data Fig. 9 | Prognostic significance of myeloid-specific HO-1. a, expression of CD163 and HO-1 in metastatic lesions of AJCC Stage III melanoma patients. Consecutive sections from lesions (LN=lymph node; s.c.: subcutaneous) of 10 patients were stained for CD163 and HO-1. Wide field images and higher magnification insets are shown centered on the same area of the tumor tissue for both markers. Lesions from patients #1 to #8 (short survival) show expression of both CD163 and HO-1 in the same areas of the tumor tissue. Lesions from patients #11 to #15 (long survival) show lack of both CD163 and HO-1 expression. For each patient, survival was computed from the date of surgery for removal of metastatic lesions. Status: DOD: dead of disease, NED: no evidence of disease. **b**, results of multivariable Cox proportional hazard model on TCGA skin cutaneous melanoma dataset ($n = 471$) were obtained through the outcome module of TIMER2.0 web server, by testing the relevance of tumor infiltrating macrophages, as identified by the M2_TIDE macrophage signature[52], and of the expression of macrophage-related genes CD163, HO-1 and CD68. Tumor stage was included as clinical covariate.

nature research

Corresponding author(s):	Antonio Sica
Last updated by author(s):	Mar 9, 2021

Reporting Summary

Nature Research wishes to improve the reproducibility of the work that we publish. This form provides structure for consistency and transparency in reporting. For further information on Nature Research policies, see our Editorial Policies and the Editorial Policy Checklist.

Please do not complete any field with "not applicable" or n/a. Refer to the help text for what text to use if an item is not relevant to your study.
For final submission: please carefully check your responses for accuracy; you will not be able to make changes later.

Statistics

For all statistical analyses, confirm that the following items are present in the figure legend, table legend, main text, or Methods section.

n/a	Confirmed	
☐	☒	The exact sample size (*n*) for each experimental group/condition, given as a discrete number and unit of measurement
☐	☒	A statement on whether measurements were taken from distinct samples or whether the same sample was measured repeatedly
☐	☒	The statistical test(s) used AND whether they are one- or two-sided *Only common tests should be described solely by name; describe more complex techniques in the Methods section.*
☒	☐	A description of all covariates tested
☐	☒	A description of any assumptions or corrections, such as tests of normality and adjustment for multiple comparisons
☐	☒	A full description of the statistical parameters including central tendency (e.g. means) or other basic estimates (e.g. regression coefficient) AND variation (e.g. standard deviation) or associated estimates of uncertainty (e.g. confidence intervals)
☐	☒	For null hypothesis testing, the test statistic (e.g. *F*, *t*, *r*) with confidence intervals, effect sizes, degrees of freedom and *P* value noted *Give P values as exact values whenever suitable.*
☒	☐	For Bayesian analysis, information on the choice of priors and Markov chain Monte Carlo settings
☒	☐	For hierarchical and complex designs, identification of the appropriate level for tests and full reporting of outcomes
☒	☐	Estimates of effect sizes (e.g. Cohen's *d*, Pearson's *r*), indicating how they were calculated

Our web collection on statistics for biologists contains articles on many of the points above.

Software and code

Policy information about availability of computer code

Data collection	BD FACSDiva Software (v8.0.1 and 6.2), ImageLab Software (4,1 BioRad), Aperio Scanscope XT digital phatology slide scanner, Olympus Fluoview FV1000 (FV10-ASW 3.0) , LASX software (3.5.7 Leica Microsystems),
Data analysis	GraphPad Prism7, BD FACSDiva Software (v8.0.1 and 6.2) and FlowJo (9.3.2, 9.9.6 and 10.5.3) software, ImageLab Software 4,1, SDS2.2.2 software, QuPath software (0.1.2), Feature Extraction Software (v10.7), Timer2.0 web server, Olympus Fluoview FV1000 (FV10-ASW 3.0), LASX software (3.5.7 Leica Microsystems), R (v3.5.1), Bioconductor (v3.8), limma R package (v3.38), biomaRt R package (v2.40), pheatmap R package (v1.0.12), ClusterProfiler R package (v3.10.1), Image Pro-Premier Software (9.2 Media Cybernetics); factoextra R package (v1.0.6) FactoMineR R package (v1.42)

For manuscripts utilizing custom algorithms or software that are central to the research but not yet described in published literature, software must be made available to editors and reviewers. We strongly encourage code deposition in a community repository (e.g. GitHub). See the Nature Research guidelines for submitting code & software for further information.

Data

Policy information about availability of data

All manuscripts must include a data availability statement. This statement should provide the following information, where applicable:

- Accession codes, unique identifiers, or web links for publicly available datasets
- A list of figures that have associated raw data
- A description of any restrictions on data availability

The data that support the findings of this study are available from the corresponding author upon reasonable request. RNA-seq raw data are reported in Suplemetary Table 1 and have been deposited at the Gene Expression Omnibus (GEO accession no. GSE167413). Datasets containing patients' clinical parameters and flow cytometry data generated during the current study are presented in the accompanying Supplementary Table 2-3.

Field-specific reporting

Please select the one below that is the best fit for your research. If you are not sure, read the appropriate sections before making your selection.

☒ Life sciences ☐ Behavioural & social sciences ☐ Ecological, evolutionary & environmental sciences

Life sciences study design

All studies must disclose on these points even when the disclosure is negative.

Sample size	For in vivo animal experiment, sample sizes were defined on the basis of our many years of experience with the experimental models used in our study, in order to detect differences of 20% or greater between the groups (10% significance level and 80% power). For in vitro experiments, no sample size power capculation was performed. A minimum of 3 biological replicates were used for each experiment. All details for each experiment is icluded in the corresponding figure legend.
Data exclusions	No data were excluded from the analysis
Replication	The experimental findings were reliably reproduced. In some instances, the results from different experiments have been pooled in others the results from one representative experiment have been shown. The number of replicates is given in the respective figure legends.
Randomization	Mice were randomized based on sex and age. For in vitro experiments, samples were randomly allocated into a control or experimental group.
Blinding	In most in vivo experiments, the investigators were unaware of the genotype of the experimental groups. Most of the in vitro analisys were not blinded but kept as unbiased as possible. For all flow cytometry, confocal and immunoistochemical analysis, every sample was processed identically by one experimenter to avoid any technical bias. Tumor cells injections were performed by the same researcher to ensure reproducible inoculations from mouse to mouse. For each studies we also include appropiate internal controls and normalization methods to control for internal bias.

Reporting for specific materials, systems and methods

We require information from authors about some types of materials, experimental systems and methods used in many studies. Here, indicate whether each material, system or method listed is relevant to your study. If you are not sure if a list item applies to your research, read the appropriate section before selecting a response.

Materials & experimental systems

n/a	Involved in the study	
☐	☒	Antibodies
☐	☒	Eukaryotic cell lines
☒	☐	Palaeontology and archaeology
☐	☒	Animals and other organisms
☐	☒	Human research participants
☒	☐	Clinical data
☒	☐	Dual use research of concern

Methods

n/a	Involved in the study	
☒	☐	ChIP-seq
☐	☒	Flow cytometry
☒	☐	MRI-based neuroimaging

Antibodies

Antibodies used	For FACS analysis, the following antibodies (clone, catalog number, source, diluition) were used: anti-human CD14-PE-CF594 (M5E2) Biolegend Cat#301851 (1/200) anti-human CD3-PerCP-Cy5.5 (UCHT1) Biolegend Cat#300430 (1/100) anti-human CD16-PE-Cy7 (3G8) Biolegend Cat#302015 (1/400) anti-human CD45-BV421 (HI30) Biolegend Cat#304032 (1/200) anti-human CD88-PE (S5/1) Biolegend Cat#344303 (1/200) anti-human CD19-PerCP-Cy5.5 (SJ25C1) Biolegend Cat#363015 (1/100) anti-human CD56-PerCP-Cy5.5 (5.1H11)Biolegend Cat#362505 (1/100) anti-human Tie-2/CD202b-Alexa Fluor 647 (33.1) Biolegend Cat#334209 (1/200) anti-human HMOX1 FITC Abcam Cat#ab69545 (1/200) Zombie Aqua Vixable Viability kit, Biolegend Cat#423102 (1/800) anti-mouse CD45-FITC (30-F11) Biolegend Cat#103108 (1/400) anti-mouse CD45-PerCP (30-F11) Biolegend Cat#103130 (1/200) anti-mouse CD45-BUV563 (30-F11) BD Horizon Cat#565710 (1/400) anti-mouse CD45.1-APC (A20) Biolegend Cat#110714 (1/200) anti-mouse CD45.2-FITC (104) Biolegend Cat#109806 (1/200)

anti-mouse CD11b-PerCp-Cy5.5 (M1/70) eBioscence Cat#45-0112-82 (1/200)
anti-mouse CD11b-PE (M1/70) Biolegend Cat#101208 (1/400)
anti-mouse CD11b-FITC (M1/70) Biolegend Cat#101206 (1/200)
anti-mouse CD11b-BV711 (M1/70) Biolegend Cat#101242 (1/600)
anti-mouse F4/80-APC (BM8) Biolegend Cat#123116 (1/100)
anti-mouse F4/80-PE (BM8) Biolegend Cat#123110 (1/200)
anti-mouse F4/80-PE-Cy7 (BM8) Biolegend Cat#123114 (1/200)
anti-mouse F4/80-BV421 (BM8) Biolegend Cat#123137 (1/100)
anti-mouse Ly6G-PE (1A8) Biolegend Cat#127608 (1/200)
anti-mouse Ly6G-BV570 (1A8) Biolegend Cat#127629 (1/100)
anti-mouse Ly6C- APC-Cy7 (HK1.4) eBioscence Cat#47-5932-82 (1/600)
anti-mouse MHCII-PE-Cy7 (M5/114.15.2) eBioscence Cat#78-5321-82 (1/200)
anti-mouse MHCII-PE (M5/114.15.2) Biolegend Cat#107607 (1/400)
anti-mouse MHCII-BV480 (M5/114.15.2) BD Horizon Cat#566088 (1/600)
anti-mouse CD11c-APC (N418) Biolegend Cat#117310 (1/100)
anti-mouse CD11c-BV605 (N418) eBioscence Cat#63-0114-82 (1/200)
anti-mouse CD8-APC (53-6.7) Biolegend Cat#100712 (1/100)
anti-mouse CD8-BUV805 (53-6.7) BD Horizon Cat#564920 (1/200)
anti-mouse CD4-PE (GK1.5) Biolegend Cat#100408 (1/200)
anti-mouse CD4-PE-Cy7 (GK1.5) Biolegend Cat#100422 (1/200)
anti-mouse CD4-BUV496 (GK1.5) BD Horizon Cat#564667 (1/100)
anti-mouse CD3-PerCP (145-2C11) Biolegend Cat#100326 (1/100)
anti-mouse CD3-BV650 (145-2C11) Biolegend Cat#100229 (1/100)
anti-mouse IFNγ-FITC (XMG1.2) Biolegend Cat#505806 (1/100)
anti-mouse IFNγ-PE (XMG1.2) BD Pharmingen Cat#554412 (1/200)
anti-mouse FoxP3-AlexaFluor 488 (MF23) BD Pharmingen Cat#560403 (1/100)
anti-mouse FoxP3-AlexaFluor 647 (MF23) BD Pharmingen Cat#560402 (1/100)
anti-mouse CD115-PE (AFS98) Biolegend Cat#135505 (1/100)
anti-mouse CD115-APC (AFS98) Biolegend Cat#135510 (1/50)
anti-mouse CD31-PE (MEC13.3) BD Pharmingen Cat#553373 (1/100)
anti-mouse TIE2 CD202b-PE (TEK4) eBioscence Cat#12-5987-81 (1/200)
anti-mouse CD88-PE (20/70) Biolegend Cat#135806 (1/200)
anti-mouse CD88-APC (20/70) Biolegend Cat#135808 (1/100)
anti-mouse CCR2-AlexaFluor 647 (SA203G11) Biolegend Cat#150603 (1/100)
anti-mouse CCR2-PE-Cy7 (SA203G11) Biolegend Cat#150612 (1/100)
anti-mouse HO-1-PE (HO-1-2) EnzoLifeSciences Cat#ADI-OSA-11PE-F (1/200)
anti-mouse CX3CR1-PE (SA011F11) Biolegend Cat#149005 (1/200)
anti-mouse CD195 (CCR5)-PE (HM-CCR5) Biolegend Cat#107005 (1/100)
anti-mouse TNF⍰-AlexaFluor 647 (MP6-XT22) BD Pharmingen Cat#557730 (1/100)
anti-mouse CD206-APC (C068C2) Biolegend Cat#141708 (1/100)
anti-mouse CD64-APC (X54-5/7.1) eBioscence Cat#17-0641-82 (1/100)
anti-mouse CD16/32-APC (93) eBioscence Cat#17-0161-82 (1/100)
anti-mouse Hematopoietic Lineage-eFluor 450 eBioscence Cat#88-7772-72 (1/400)
anti-mouse CD34 FITC (RAM34) BD Pharmingen Cat#560238 (1/100)
anti-mouse Gr1-FITC (RB6-8C5) BD Pharmingen Cat#553127 (1/50)
anti-mouse CD44-FITC (IM7) Biolegend Cat#103006 (1/100)
anti-mouse CD62L-APC (Mel-14) BD Pharmingen Cat#553152 (1/100)
anti-mouse CD62L-BV570 (Mel-14) Biolegend Cat#104433 (1/100)
anti-mouse SiglecF-FITC (S17007L) Biolegend Cat#155504 (1/100)
anti-mouse SiglecF-AlexaFluor 700 (E50-2440) BD Bioscence Cat#562680 (1/50)
anti-mouse Ki67-APC (16A8) Biolegend Cat#652405 (1/100)
anti-mouse VEGFR-PE-Cy7 (Avas12) Biolegend Cat#136414 (1/200)
anti-mouse CD163-Super Bright 702 (TNKUPJ) eBioscence Cat#67-1631-82 (1/100)
anti-mouse E-Cadherin-BV421 (DECMA-1) Biolegend Cat#147319 (1/100)
goat policlonal anti-C3aR (D-20) Santa Cruz Biotechnology Cat#sc-14624 (1/100)
rabbit anti-pSTAT1 (58D6) Cell Signaling Cat#9167 (1/200)
rabbit anti-pSTAT3 (M9C6) Cell Signaling Cat#4113 (1/200)
rabbit anti-pSTAT6 (D8S9Y) Cell Signaling Cat#56554 (1/200)
Nrf2 rabbit polyclonal antibody ThermoFisher Cat#PA5-27882 (1/100)
VEGF rabbit polyclonal antibody (SP07-01) ThermoFisher Cat#MA5-32038 (1/100)
Vimentin rabbit monoclonal antibody (SP20) ThermoFisher Cat#MA5-14564 (1/100)
N-Cadherin rabbit monoclonal antibody (3B9) ThermoFisher Cat#33-3990 (1/100)
anti-HIF1⍰⍰rabbit monoclonal antibody (16H4L13) ThermoFisher Cat#700505 (1/100)
donkey anti-goat Alexa Fluor® 647-conjugated antibody ThermoFisher Cat#A-21447 (1/500)
goat anti-rabbit Alexa Fluor® 488-conjugated antibodies ThermoFisher Cat#A-11008 (1/500)
goat anti-rabbit Alexa Fluor® 647-conjugated antibodies ThermoFisher Cat#A27040 (1/500)
LIVE/DEAD™ Fixable Violet Dead Cell Stain Kit Thermo Fisher, Cat#L34960 (1/1000)

For in vivo studies, the following antibodies were used:
Rat Anti-Mouse CD4 Monoclonal Antibody Clone GK1.5 BioXcell Cat#BE0003-1 0.3 mg/mouse
Rat Anti-Mouse CD8a Monoclonal Antibody Clone 2.43 BioXcell Cat#BE0061 0.3 mg/mouse
Rat Anti-Mouse PD-1 Monoclonal Antibody clone RPM1-14 BioXcell Cat#BE0146 100 µg/mouse
anti-CSFR1 antagonist (kindly donated by Dr. Carola Ries, Roche Diagnostic GmbH, Penzberg, Germany)

For IHC analysis, murine tissues were stained with the following primary antibody:
CD31 (0.5µg/ml PECAM-1, Pharmingen, San Diego, CA), F4/80 (clone CI:A3-1 BioRad Cat#MCA497R 1/500), HO-1 (BioRad

Cat#4915-1050 1/500). Rat- on-Mouse HRP polymer kit (RT517H, Biocare Medical) and MACH1 Universal HRP-Polymer detection (M1U539 G, Biocare Medical) were used as secondary antibody.
Human tissues were stained with the following primary antibody: CD3 (NCL-L-CD3-PS1, Leica Biosystems), CD68 (M0814, Dako), CD163 (NB110-59935, Novus Biologicals) and HMOX1 (ab13248, Abcam).

For confocal microscopy, murine tissues were stained with rabbit anti-mouse/human HO-1 (1µg/ml BioRad Cat#4915-1050), rat anti-mouse F4/80 (1µg/ml BioRad Cat#MCA497R), rabbit anti-mouse CD31 (0.5µg/ml PECAM-1, Pharmingen, San Diego, CA) followed by Alexa Fluor® 488-conjugated goat anti-rabbit IgG (ThermoFisher Cat#A-11008 1/1000) and Alexa Fluor® 647-conjugated goat anti-rat IgG antibody (ThermoFisher Cat#A21-247 1/1000). Nuclei were counterstained with DAPI (Invitrogen Cat#D1306). For in vivo vascular permeability analysis, FITC–labeled 40-kDa dextran (0.25 mg/mouse; ThermoFisher Scientific-Life Technologies Cat#D1845) was administered intravenously by retroorbital injection into anesthetized MN/MCA1–bearing mice. Following primary were used: rat anti-mouse CD31 (#MEC 13.3, 0.5µg/ml; BD Biosciences), Cy3TM-labelled anti-⍰-SMA (#1A4, 2µg/ml; Sigma-Aldrich) and rabbit anti-Collagen IV (#PA1-28534, 1µg/ml; ThermoFisher Scientific). A goat anti-rat conjugated with Alexa Fluor® 647 (ThermoFisher Scientific Cat#A21-247) and a goat anti-rabbit conjugated with Alexa Fluor® 532 (ThermoFisher Scientific Cat#A11-009) were respectively used to detect CD31 and Collagen IV.

Validation	Antibodies were from commercial vendors as specified above. Specificity was based manufacturers provided description and data sheets and was confirmed in the literature. Any information regarding the validation performed by the manufacturer can be retrieved on the manufacturers' websites. No further validation was performed. For each antibodies, the diluition was optimized in the lab on relevant cellls and tissues prior to usage

Eukaryotic cell lines

Policy information about cell lines

Cell line source(s)	The following cell lines were used: 3-MCA derived mycoplasma-free sarcoma cell line MN/MCA1, B16/F10 and K1735M2 melanoma cells. B16/F10 cells were purchased from ATCC (Manassas, VA). K1735-M2 cells were kindly provided by Dr.ssa L. Carminati (Laboratory of Tumor Microenvironment, Istituto di Ricerche Farmacologiche Mario Negri IRCCS, Bergamo, Italy). 3-MCA derived mycoplasma-free sarcoma cell line MN/MCA1 derived from a stock periodically renewed through primary cells isolated from tumor implanted in WT mice
Authentication	None of the cell lines were authenticated in these studies, but low passage number cell lines were utilized.
Mycoplasma contamination	All cell lines were routinely tested for mycoplasm contamination. All the cell lines are mycoplasma-free.
Commonly misidentified lines (See ICLAC register)	No commonly misidentified cell lines were used.

Animals and other organisms

Policy information about studies involving animals; ARRIVE guidelines recommended for reporting animal research

Laboratory animals	Mice used in this study were 8-12 weeks of age; both males and females were used. Individual experiments were age and sex matched. Wild-type C57BL/6J mice and C3H/HeN mice were obtained from Charles River Laboratories (Calco, Italy). p50 NF-kB deficient mice were available in the laboratory. Homozygous C3 mutant mice (B6;129S4-C3tm1Crr/J) were purchased from Jackson Laboratories (Bar Harbor, Maine, USA). The NFKB1flox/flox (p50flox) mice was recently generated in our laboratory. p50fl/fl mice were crossed with B6.129P2-Lyz2tm1(cre)Ifo/J mice (Jackson Laboratories, Bar Harbor, Maine, USA) to generate p50fl/fl Lyz2-Cre mice. Hmox1fl/fl and Hmox1fl/fl Lyz2-Cre mice were kindly donated by Dr. Barbara Wegiel (Beth Israel Deaconess Medical Center, Harvard Medical School, Boston). All colonies were housed and bred in the SPF animal facility of Humanitas Clinical and Research Center in individually ventilated cages. Mice were randomized on the basis of sex, age and weight. Mice were housed in 12-hour/12-hour light/dark cycle at an ambient temperature of 22 +/- 1°C with humidity 52-55%.
Wild animals	the study did not involve wild animals
Field-collected samples	the study did not involve field-collected samples
Ethics oversight	All procedures involving mice handling and care conformed to protocols approved by the Humanitas Clinical and Research Center (Rozzano, Milan, Italy) in compliance with national (D.L. N.116, G.U., suppl. 40, 18-2-1992 and N. 26, G.U. March 4, 2014) and international law and policies (EEC Council Directive 2010/63/EU, OJ L 276/33, 22-09-2010; National Institutes of Health Guide for the Care and Use of Laboratory Animals, US National Research Council, 2011). The study was approved by the Italian Ministry of Health (approval number 97/2014-PR and 25/2018-PR).

Note that full information on the approval of the study protocol must also be provided in the manuscript.

Human research participants

Policy information about studies involving human research participants

Population characteristics	Human peripheral blood leukocytes were collected from Stage IIIC, IIID and IV (AJCC melanoma staging system, eight edition) undergoing surgical treatment for metastatic melanoma at Fondazione IRCCS Istituto Nazionale dei Tumori, Milan between

	November 2001 and September 2003. Populations characteristics: discovery set + confirmation set (n=92) age: median=56, range=26-75; discovery set (n=47) age: median=52, range=27-75; confirmation set (n=45) age: median=57.5, range 26-73. Discovery set + confirmation set gender: M=55, F=37; discovery set gender: M=29, F=18; confirmation set gender: M=26, F=19. No genotypic information was available
Recruitment	The participants were recruited as a consecutive series of patients admitted to Fondazione IRCCS Istituto Nazionale dei Tumori, Milan, for surgical treatment of advanced melanoma. The only criteria for recruitment were: diagnosis of cutaneous melanoma and AJCC clinical stage III or IV. No additional self-selection bias or other biases were present.
Ethics oversight	Samples from the cohorts described in this study were obtained based on informed consent and the study was conducted according to the Declaration of Helsinki Principles and following approval by the Ethics Committe of Fondazione IRCCS Istituto Nazionale dei Tumori, Milan.

Note that full information on the approval of the study protocol must also be provided in the manuscript.

Flow Cytometry

Plots

Confirm that:

☒ The axis labels state the marker and fluorochrome used (e.g. CD4-FITC).

☒ The axis scales are clearly visible. Include numbers along axes only for bottom left plot of group (a 'group' is an analysis of identical markers).

☒ All plots are contour plots with outliers or pseudocolor plots.

☒ A numerical value for number of cells or percentage (with statistics) is provided.

Methodology

Sample preparation	Human peripheral mononuclear cells (PBMC) were obtained through a Ficoll density gradient centrifugation (Ficoll-Paque PLUS, GE Healthcare). Multicolor staining for cell populations was performed on cryopreserved samples; cells were thawed in RPMI medium supplemented with 10% human serum (HS); 2×106 lymphocytes were resuspended in 100 μL of staining buffer (PBS plus 2% FBS) and incubated with FcR Blocking Reagent (Miltenyi Biotec), with antibodies against the indicated cell surface markers and Zombie Aqua (Fixable viability dye, Biolegend) in Staining buffer (PBS, 2% FBS) for 30 minutes at +4°C. Cell permeabilization was obtained with a Cytofix/Cytoperm™ Fixation/Permeabilization Solution Kit (BD Pharmingen) according to manufacturer's instructions. Primary tumors were cut into small pieces, disaggregated with 0.5 mg ml−1 collagenase IV and 150 U ml−1 DNase I in RPMI-1640 for 30 min at 37 °C and filtered through strainers. Macroscopic lung metastatic lesions were removed with a tweezer. The isolated pulmonary nodules were finely minced, disaggregated with 0.5 mg ml−1 collagenase IV and 150 U ml−1 DNase I in RPMI-1640 for 30 min at 37 °C and filtered through Falcon strainers (70 μm). Splenocytes were collected from spleen after disaggregation and filtration through Falcon strainers (70 μm). Liver were removed, cut into small pieces, and gently mashed through a cell strainer (70 μm); then, the leukocyte population was enriched by a 35% Percoll gradient (Sigma). BM cells were isolated from the tibias and femurs of tumour-free and tumour-bearing mice. Whole blood samples were collected from the facial vein or heart in EDTA-coated collection tubes and were directly processed using a standardized red blood cell lysis protocol. Cells were re-suspended in HBSS (Hank's balanced salt solution, Lonza) supplemented with 0.5% BSA (Sigma Aldrich) and the staining was performed at 4°C for 20 minutes with specific antibodies. Cell viability was determined by LIVE/DEAD™ Fixable Violet Dead Cell Stain Kit (Thermo Fisher), negative cells were considered viable. For intra-cellular staining Foxp3/Transcription Factor Staining Buffer Set (eBioscence) were used according to the manufacturer's instruction. TNFa and IFNg expression was analyzed by flow cytometry upon 4h treatment with Brefeldin (5μg ml−1), PMA (50ng ml−1) and ionomycin (1μg ml−1). Tumor-associated macrophages (TAMs), isolated 3-4 weeks after tumor implantation, were enriched by positive selection with CD11b microbeads according to the manufacturer's instructions (MACS, Miltenyi Biotec). CD11b+ cells were stained (CD45-PerCP, F4/80-APC, CD88-PE) and sorted to obtained high-purity TAMs populations (F4/80highC5aRhigh and F4/80lowC5aRlow).
Instrument	BD FACSCanto™ II, BD LSRFortessa™ , BD FACSymphony™, 10-color Gallios (Beckman Coulter), BD FACSAria cell sorter
Software	BD FACSDiva Software (v8.0.1 and 6.2) and FlowJo Software (9.3.2, 9.9.6, 10.5.3)
Cell population abundance	Post-sort cells were ≥90% pure, as determined by reanalysing by FACS a fraction of sorted cells.
Gating strategy	A relevant gating strategy for HO-1 expression in peripheral blood monocyte subsets are described in Extended Data Fig. 7a. A relevant gating strategy for murine F4/80hi and F4/80lo TAMs is described in Supplementary Figure 1.

☒ Tick this box to confirm that a figure exemplifying the gating strategy is provided in the Supplementary Information.

This checklist template is licensed under a Creative Commons Attribution 4.0 International License, which permits use, sharing, adaptation, distribution and reproduction in any medium or format, as long as you give appropriate credit to the original author(s) and the source, provide a link to the Creative Commons license, and indicate if changes were made. The images or other third party material in this article are included in the article's Creative Commons license, unless indicated otherwise in a credit line to the material. If material is not included in the article's Creative Commons license and your intended use is not permitted by statutory regulation or exceeds the permitted use, you will need to obtain permission directly from the copyright holder. To view a copy of this license, visit http://creativecommons.org/licenses/by/4.0/